TU Delft

Delft University of Technology

Document Version
Final published version

Licence
CC BY

Citation (APA)
Krempus, D., Beltrame, F., Vos, R., Colonna, P., & de Servi, C. M. (2026). Feasibility Study of an Organic Rankine Cycle Waste Heat Recovery System for the Engines of a Partial-Turboelectric Aircraft. *Journal of Engineering for Gas Turbines and Power*, *148*(11), Article GTP-25-1623. https://doi.org/10.1115/1.4072320

Important note
To cite this publication, please use the final published version (if applicable).
Please check the document version above.

Copyright
In case the licence states “Dutch Copyright Act (Article 25fa)”, this publication was made available Green Open Access via the TU Delft Institutional Repository pursuant to Dutch Copyright Act (Article 25fa, the Taverne amendment). This provision does not affect copyright ownership.
Unless copyright is transferred by contract or statute, it remains with the copyright holder.

Sharing and reuse
Other than for strictly personal use, it is not permitted to download, forward or distribute the text or part of it, without the consent of the author(s) and/or copyright holder(s), unless the work is under an open content license such as Creative Commons.

Takedown policy
Please contact us and provide details if you believe this document breaches copyrights.
We will remove access to the work immediately and investigate your claim.

This work is downloaded from Delft University of Technology.

Check for updates

ASME Journal of Engineering for Gas Turbines and Power
Online journal at:
https://asmedigitalcollection.asme.org/gasturbinespower

Dabo Krempus
Propulsion and Power,
Faculty of Aerospace Engineering,
Delft University of Technology,
Kluyverweg 1,
Delft 2629HS, The Netherlands

Fabio Beltrame
Propulsion and Power,
Faculty of Aerospace Engineering,
Delft University of Technology,
Kluyverweg 1,
Delft 2629HS, The Netherlands

Roelof Vos
Flight Performance and Propulsion,
Faculty of Aerospace Engineering,
Delft University of Technology,
Kluyverweg 1,
Delft 2629HS, The Netherlands

Piero Colonna
Propulsion and Power,
Faculty of Aerospace Engineering,
Delft University of Technology,
Kluyverweg 1,
Delft 2629HS, The Netherlands

Carlo Maria De Servi
Propulsion and Power,
Faculty of Aerospace Engineering,
Delft University of Technology,
Kluyverweg 1,
Delft 2629HS, The Netherlands;
Flemish Institute for Technological Research
(VITO), Boeretang 200,
Mol 2400, Belgium
e-mail: c.m.deservi@tudelft.nl

Feasibility Study of an Organic Rankine Cycle Waste Heat Recovery System for the Engines of a Partial-Turboelectric Aircraft

This work presents a study on a novel combined-cycle turbofan (CC-TF) engine concept consisting of a turbofan engine and an organic Rankine cycle (ORC) bottoming unit. The study aims to identify if benefits in terms of mission fuel consumption can be derived from the CC-TF engine if compared to a simple-cycle turbofan engine with entry into service (EIS) in the year 2035 for the test case of a partial-turboelectric aircraft. For this purpose, a multidisciplinary simulation framework is employed, incorporating models of the engine, the distributed propulsion (DP) system, the ORC unit, the heat exchangers, as well as a simplified model of the aircraft to perform mission analysis. A propulsion system design for minimum fuel consumption is obtained by coupling the simulation framework with an optimizer. The results suggest that fuel savings of around 4% are possible with the CC-TF concept if compared to the benchmark engine, for the test case of a partial-turboelectric aircraft. The ORC system contributes approximately one-fifth of the required electrical power demand and features a mass-specific power of approximately 1 kW/kg. The estimated thrust-specific fuel consumption of the partial-turboelectric propulsion system adopting the CC-TF engine is 13.5 mg/N·s, which is approximately 6% lower than that of the benchmark. The CC-TF engine benefits from the ORC system in two ways. First, the contribution of the ORC system to shaft power production reduces the required fuel mass flow rate. Second, the thermal energy transfer to the engine bypass stream from the condensers of the ORC system increases both the engine propulsive efficiency and the specific thrust if compared to a simple-cycle turbofan engine with a similar bypass ratio. [DOI: 10.1115/1.4072320]

1 Introduction

The thermal efficiency of contemporary aero-engines is approximately 50%. This implies that half of the chemical energy resulting from fuel combustion is dissipated into the environment in the form of a hot exhaust gas stream. Enhancements in the thermal efficiency of traditional gas turbines can be attained by increasing turbine inlet temperature (TIT) and overall pressure ratio (OPR). Nevertheless, achieving further efficiency gains via these methods has become increasingly challenging due to material constraints and stringent emission regulations [1]. To overcome these limitations, modifications to the thermodynamic cycle are being explored. Various concepts, including architectures incorporating recuperation and/or intercooling, as well as combined-cycle configurations, have been extensively investigated in the past [2–4]. However, these cycle configurations, commonplace in the power sector, have yet to be implemented in aircraft propulsion systems. Notably, organic Rankine cycle (ORC) bottoming units have been successfully integrated into medium-power capacity stationary gas turbines [5]. ORC waste heat recovery (WHR) systems have also found application on vessels and have undergone comprehensive testing as a means to enhance the fuel efficiency of long-haul truck engines [5].

Only a few studies analyzed the effect of recovering otherwise wasted thermal energy from aero-engines with an ORC WHR system. The first investigation on the feasibility of integrating an ORC WHR system with a CFM56 turbofan engine is reported in Ref. [6]. The authors analyzed the retrofit of an existing engine with the addition of a WHR system based on an air-cooled subcritical recuperated ORC configuration using R245fa as the working fluid. In their design, the evaporator is integrated into the walls of the engine core nozzle, and the condenser is integrated into the engine air intake lip. The ORC turbogenerator and the pump are integrated into the engine pylon and nacelle, respectively. The ORC system is designed to provide 200 kW of electrical power to the electrically driven air compressor of the environmental control system. The

Manuscript received October 9, 2025; final manuscript received June 7, 2026; published online August 17, 2026. Assoc. Editor: Mauro Venturini.

Copyright © 2026 by ASME; reuse license CC-BY 4.0

Downloaded from asmedigitalcollection.asme.org/gasturbinespower/article-pdf/148/11/111002/7625683/gtp-25-1623.pdf by Technische Universiteit Delft - Bibliotheek user on 20 October 2026

study is solely based on thermodynamic on-design calculations, and component sizing is not included. A mass of 430 kg is assumed for the WHR system per engine. The fuel-saving potential for a short-range flight is estimated to be 0.9%.

Reference [7] investigated a retrofitting scenario of integrating an ORC WHR system with a 2 MW-class turboprop engine powering a regional aircraft. A WHR system based on an air-cooled subcritical nonrecuperated ORC configuration using R245fa as the working fluid is modeled, including the sizing of both plate-fin heat exchangers. The condenser is housed in a separate ram-air duct, and the evaporator is located in the exhaust duct of the engine. Simplified 0D modeling of the ram-air duct is conducted, and it is concluded that the thermal energy transferred from the condensing working fluid to the ram-air generates sufficient thrust to overcome the drag caused by the air intake, duct, and heat exchanger core. On and off-design simulations are carried out, and the system is optimized to provide maximum heat recovery during cruise (CR). No details regarding the optimization procedure are given. Furthermore, it is determined that transferring the ORC turbine power directly to the low-pressure shaft of the engine yields the largest fuel savings. The envisaged combined-cycle engine results in a reduction of mission fuel mass of 1.7% for a 300 NM trip in comparison with the benchmark engine. The exhaust gas temperature of the engine is 750 K, and the ORC turbogenerator provides 100 kW of shaft power. The designed WHR unit has a mass-specific power of 0.33 kW/kg. Additionally, based on the assumption of an ORC turbine mass-specific power of 0.5 kW/kg, the ORC turbine is identified as the major contribution to ORC system mass (70%) followed by the condenser (20%).

The work documented in Refs. [8] and [9] investigated the integration of a supercritical CO_2 WHR system with turbofan engines for long-range aircraft. Both studies consider a recuperated cycle configuration with the heater located in the engine core exhaust duct and the cooler in the engine bypass duct. Suitable WHR system designs to provide a turbine power output of around 1000 kW were identified by means of parametric studies including heat exchanger sizing. The turbofan engines considered in Refs. [8] and [9] have an exhaust gas temperature of 615 K and 780 K, respectively. The latter value is considerably higher due to the lower technology level and therefore thermodynamic efficiency of the engine. Downsizing of the engine due to the contribution of the WHR system was not considered. Despite the similar configurations (high bypass turbofan engine, air-cooled recuperated cycle architecture, CO_2 as the working fluid, and same cooler and heater placement), estimated component weight differs substantially and, as a result, an opposing outcome is obtained regarding fuel mass saving potential. The authors of Ref. [9] reported a fuel mass reduction of 1.9%, while those of Ref. [8] concluded that the efficiency increase of the combined-cycle engine is insufficient to counter the added system weight.

The addition of an ORC WHR unit to the internal combustion engine of a parallel-hybrid electric drive train for a small general-aviation aircraft was analyzed in Ref. [10]. The performance of a WHR unit based on a fuel-cooled subcritical nonrecuperated ORC configuration is investigated for five different hydrofluoroolefins as the working fluid. In contrast to the studies reported in Refs. [6] and [7], the prime mover is downsized so that the combined-cycle hybrid drive train fulfills the specified power requirement. The investigation is carried out for three different aircraft with a power requirement of the combined-cycle engine ranging from 100 to 300 kW. Component sizing is not performed, and the impact of added system weight is investigated by means of a parametric study. Only the on-design performance of the system is analyzed. For three investigated aircraft types, an ORC mass-specific power above 0.8 kW/kg leads to a fuel burn reduction of around 13%.

All these studies indicate a different level of possible fuel savings by integrating the engine with a WHR unit compared to their simple-cycle counterparts, ranging from 1% to 13%. A possible reason for the large spread is that they differ in the level of modeling fidelity, and that component sizing and airframe integration are only partially considered.

More recent work by the authors aimed at closing this knowledge gap [11,12]. Part of this effort is devoted to the development of a multidisciplinary simulation framework to investigate ORC WHR systems onboard aircraft. This framework, named ARENA (airborne thermal energy harvesting for aircraft), is implemented in PYTHON and includes modules for gas turbine and ORC performance simulations, ORC turbine and heat exchanger (HEX) preliminary design, as well as aircraft design and performance simulation. In Ref. [11], this preliminary design framework was employed to study a simple application scenario involving an aircraft auxiliary power unit (APU) whose performance is enhanced with an ORC WHR system to provide power on the ground. A nonrecuperated fan-air-cooled cycle architecture using cyclopentane as the working fluid was adopted for the WHR system. The combined-cycle system was placed in the tailcone of the A320-like aircraft, and corresponding size limitations were applied to the design of the heat exchangers. The results indicated that with such a combined-cycle APU (CC-APU), fuel consumption associated with the provision of ground power could be reduced by 50% when compared to a current-day single-cycle APU. However, due to the limited impact of the APU fuel consumption on ground compared to the fuel consumption during flight, the CC-APU enables a reduction of overall mission fuel mass of 0.5% in the case of a short-range flight. Condenser fan power consumption, along with the pressure drop on the cooling air side, was identified as the most limiting factor to CC-APU performance. The optimized CC-APU design provided 250 kW of shaft power, of which approximately one-fifth was provided by the ORC turbogenerator. The ORC WHR unit had a mass-specific power of 1.7 kW/kg.

This work gave a first insight into system design requirements, highlighted differences in the design compared to stationary ORC WHR systems, and allowed the formulation of preliminary design guidelines for airborne ORC WHR units. Furthermore, the importance of considering size limitations to achieve a realistic estimation of combined-cycle performance was highlighted. In a following research work [12], the adoption of a combined-cycle turboshaft (CC-TS) engine consisting of a turboshaft engine and an ORC WHR unit onboard a short-range fully turboelectric aircraft was investigated. In this work, a ram-air-cooled nonrecuperated ORC configuration using cyclopentane as the working fluid was adopted. The ORC WHR unit was integrated with the turboshaft engine in the nacelle, which was mounted to the tail of the fuselage with pylons. The ORC condensers were placed inside ram-air ducts on the sides of the nacelle that draw in ambient air. The on-design operation of the ORC WHR unit during cruise was analyzed by considering the change in aircraft drag due to the added ram-air ducts and condensers, as well as the resizing of the aircraft due to the heavier power plant. The optimized CC-TS design reduced overall mission fuel consumption by 1.5%. The ORC WHR unit provided 335 kW of electrical power, which covered approximately 7% of the total power requirement of a single CC-TS unit. Furthermore, the results showed that heat addition to the ram air can produce sufficient thrust to completely offset the drag imposed by the duct and the condenser. In particular, heat exchanger volume limitations and drag imposed on the aircraft are identified as the most constraining factors for CC-TS performance.

The major limitation of ORC WHR system performance concerns the rejection of thermal energy associated with the condensation of the working fluid. In the case of the CC-TS concept, the condensers are placed inside ram-air ducts. According to the results reported in Ref. [12], the thrust produced by heat addition to the ram air balances the additional drag due to the heat exchanger, the ducting, and the intakes, resulting in a net zero force acting on the aircraft. However, the enthalpy available for thrust production caused by the expansion of the air through the duct increases if thermal energy is transferred to a compressed gaseous stream. Simple calculations show that at a typical fan pressure ratio of 1.5, transferring 80 kW of thermal power per kg/s to the air stream (an amount similar to the value obtained for the ram-air ducts of the CC-TS concept) increases propulsive efficiency by 30% in absolute terms, assuming that the heat

Downloaded from asmedigitalcollection.asme.org/gasturbinespower/article-pdf/148/11/111002/7625683/gtp-25-1623.pdf by Technische Universiteit Delft - Bibliotheek user on 20 October 2026

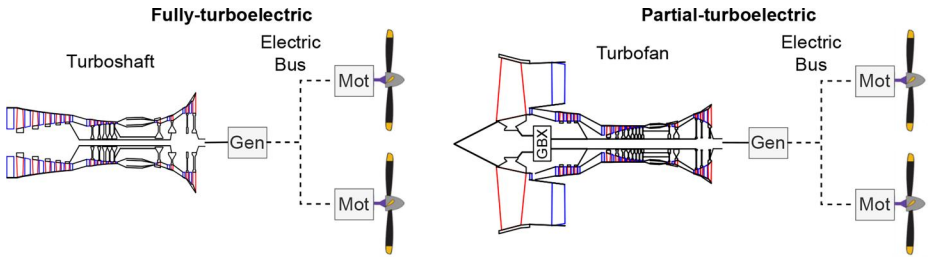


Fig. 1 Schematics of the fully turboelectric and partial-turboelectric powertrain architectures

exchanger causes no pressure loss. Propulsive efficiency is defined as the net thrust power divided by the power required to compress the air. This observation is the basis of the research regarding the combined-cycle turbofan (CC-TF) engine concept, whereby the condensers are integrated into the engine bypass duct downstream of the fan.

Adopting this engine configuration affects the overall propulsion system architecture of the aircraft. Contrary to the fully turboelectric architecture [12] (see Fig. 1), the study documented here is about the analysis of a partial-turboelectric architecture where the thrust is provided both by the CC-TF engines and by an under-the-wing distributed propulsion (DP) system composed of electrically driven ducted fans (see Fig. 1). In this work, to clearly distinguish between the two turboelectric architectures, the term fully turboelectric is used instead of turboelectric.

Examples of partial-turboelectric aircraft concepts are those studied by NASA, namely, the STARC-ABL [13] and the SUSAN [14] concepts. The top-level aircraft requirements (TLARs) of both concepts are similar to those of the Airbus A320 and employ turbofan engines to generate both thrust and electrical power, which is delivered to electric propulsors. In the case of the STARC-ABL concept, two under-the-wing-mounted turbofan engines provide electrical power to a fan located in the aftbody of the aircraft. It is reported that a fuel saving of 7% to 12% with respect to a conventional aircraft of the same technology level is achievable with simple-cycle turbofan engines. Furthermore, while the aircraft maximum takeoff mass increases due to larger wing and empennage surfaces, the propulsion system mass is reduced, since electric motors do not suffer from power lapse with increasing altitude and speed, allowing for the downsizing of the turbofan engines. The aft-fan provides approximately one-third of the required cruise thrust. The SUSAN concept employs a single tail-mounted turbofan engine, which provides 20 MW of electrical power to a distributed propulsion system located under the wings. The turbofan engine supplies 35% of the total thrust during cruise. The aircraft achieves a fuel consumption reduction of 27% if compared to the Boeing B737-800.

The aircraft considered in this work is analogous to the ONERA Dragon fully turboelectric aircraft concept [15]. Two engines housed in pods at the aft of the aircraft provide electric power to a DP system, which consists of electrically driven ducted fans, mounted under the wings. The objective of this research is to analyze the performance of two partial-turboelectric aircraft configurations in which the engines are either simple-cycle turbofans (reference aircraft) or CC-TF engines (CC-TF aircraft). The ARENA framework is used to identify preliminary fuel-optimized designs for both propulsion system concepts.

2 Methodology

The ARENA framework enables preliminary design optimization and performance evaluation of simple-cycle and combined-cycle aero engines and has been introduced in previous studies [12]. The framework is modular and leverages the PYTHON library OPENMDAO [16] to connect all submodules of a system model.

2.1 Engine Architecture. A geared two-spool turbofan engine serves as the prime mover of the reference and the CC-TF aircraft. In the case of the CC-TF engine, an ORC WHR unit recovers thermal energy from the gas turbine. Figure 2 depicts the schematic of the CC-TF engine nacelle, which is attached to the tail cone of the fuselage by means of a pylon. In the case of the simple-cycle turbofan engine, the same integration and mounting architecture is assumed, except for the missing heat exchangers. The process flow diagram of the CC-TF is depicted in Fig. 3, while the extended design structure matrix (XDSM) of the CC-TF aircraft system model containing all major modules is shown in Fig. 4. The XDSM indicates dependencies between components with the thick gray lines, and the thin black line indicates the computational flow. The exchange of dependent variables between disciplines is indicated with gray boxes. The white boxes in the top row of the diagram indicate the required user input data.

The CC-TF concept features three generators that provide electrical power to the distributed propulsion system. To ensure system redundancy and reduce overall diameter, two generators are used to extract power from the low-pressure spool of the gas turbine engine instead of one, as shown in Fig. 2. The third generator is connected to the ORC turbine, thus forming the ORC turbogenerator assembly. A single annular evaporator is located in the S-shaped annular exhaust duct of the core flow. After exiting the low-pressure turbine (LPT), the exhaust air is diverted outward, passes through the evaporator, and turns back toward the exit, forming a ring-shaped axial nozzle. This arrangement increases the evaporator heat transfer area while keeping the engine frontal area small. Additionally, it allows for an efficient integration of the electric generators. Turboprop/turboshaft engines of the Pratt & Whitney PT6 and General Electric H-series families adopt a similar configuration of the exhaust duct and have been proposed as the basis for the development of recuperated engines with annular-shaped recuperators [17] and, in a more recent study, of a water-enhanced turbofan engine [18]. The aerodynamic design of the exhaust duct presents a challenge with respect to the minimization of aerodynamic losses due to the sharp flow turning. Nevertheless, "pressure loss levels equivalent to, or better than straight-out exhausts" are possible if the ducting is carefully designed [19]. In this work, a relative pressure loss of 1.5% is taken, and this assumption is based on the preliminary design of a recuperated engine with similar ducting [17]. Eight condensers are arranged according to an octagonal pattern inside the bypass duct of the engine, see Fig. 2. To reduce engine frontal area, the condensers are tilted with respect to the radial direction by an angle θ_{cond}. Each condenser has the same size and exchanges the same amount of energy with the airflow.

2.2 Aircraft Aerodynamics, Mass, and Performance. The estimation of aircraft mass and mission analysis is performed in the module named *9:aircraft* of Fig. 4. This numerical procedure includes the evaluation of (1) lift coefficient (C_L) and drag coefficient (C_D), (2) maximum takeoff mass (m_{mto}), (3) mission fuel mass (m_{fuel}), (4) required equivalent output power of the electrical generator at the rolling-takeoff (RTO) operating point ($\dot{W}_{rto,eq}$) and required wing area (S_{ref}), (5) required power output of the electrical generator and required turbofan thrust during CR, RTO, and sea-level-static (SLS) conditions, and (6) cruise altitude (h_{cr}).

The drag polar of the aircraft is expressed using the three-term equation $C_D = C_{D,min} + K_L(C_L - C_{L,min})^2$, as detailed in Ref. [20].

Downloaded from asmedigitalcollection.asme.org/gasturbinespower/article-pdf/148/11/111002/7625683/gtp-25-1623.pdf by Technische Universiteit Delft - Bibliotheek user on 20 October 2026

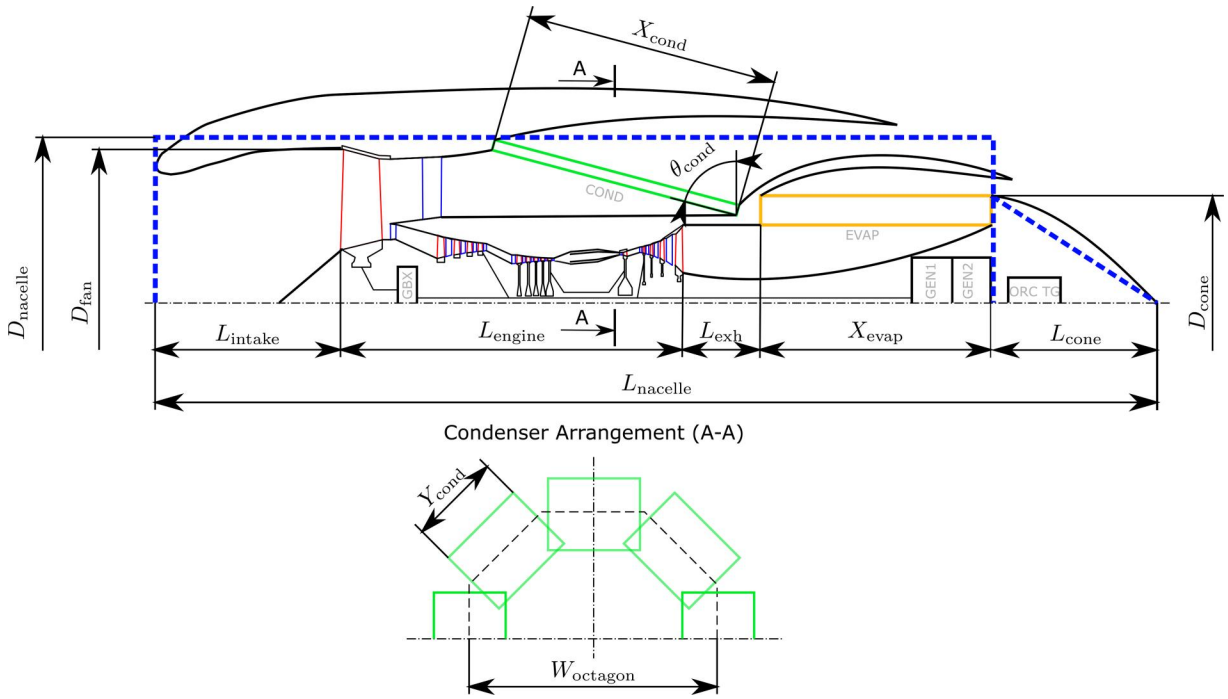


Fig. 2 Schematic of the CC-TF engine concept, including major dimensions and a cut plane (A–A) showing the condenser arrangement. The thick dashed line indicates the simplified geometry used for nacelle sizing. GBX: gearbox. COND: condenser of the ORC system. EVAP: evaporator of the ORC system. GEN: electrical generator. ORC TG: turbogenerator of the ORC system. The piping and feed pump of the ORC system are omitted. (Color version online.)

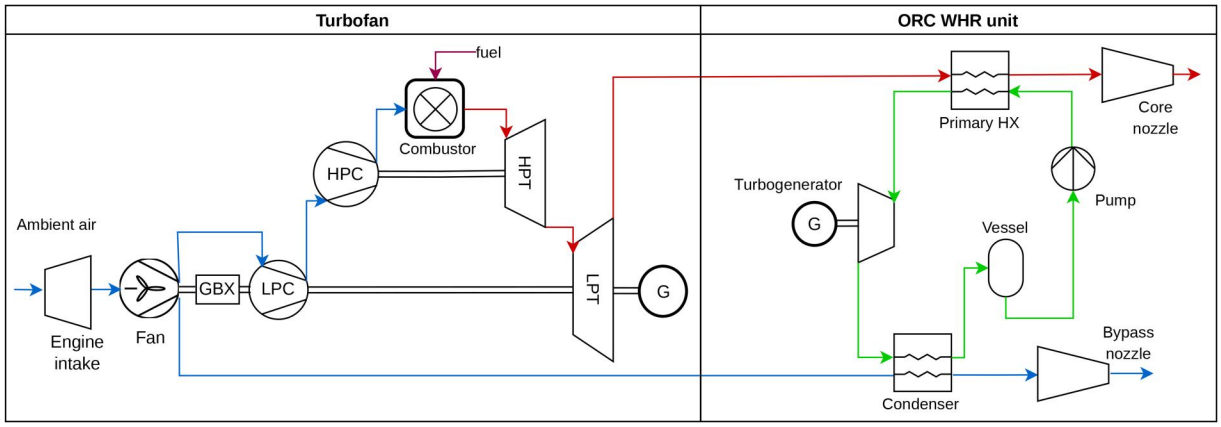


Fig. 3 Process flow diagram of the CC-TF configuration

The parameter $C_{D,min}$ is estimated to be equal to the zero-lift drag coefficient of the two-term drag polar, approximated through the methodology outlined in Ref. [21]. The values of the parameters K_L and $C_{L,min}$ are determined with two additional equations: (1) $((dL/D)/dC_L)_{cr} = 0$, assuming cruise at the maximum lift-to-drag ratio (L/D), and (2) $C_D^* = f(C_L^*)$, where $C_L^* = 0.47$ and $C_D^* = 0.0273$ are estimated for the ONERA Dragon at midcruise conditions based on data provided in Ref. [15]. The values of the derived parameters are $C_{D,min} = 0.0183$, $K_L = 0.0937$ and $C_{L,min} = 0.160$. The ram-air duct net drag affects the value of $C_{D,min}$, which results in a horizontal shift of the drag polar. The calculation of the drag polar takes into account both the nacelle and the pylon drag. For the original ONERA Dragon aircraft, the corresponding drag coefficient is estimated at approximately five drag counts, based on the method described in Sec. 2.6. In the case of the CC-TF aircraft, the variation of the nacelle drag coefficient with engine size with respect to the value calculated for the ONERA Dragon baseline is considered and accounted for as a change in zero-lift drag.

Estimating the mass of turboelectric and hybrid-electric aircraft configurations proves challenging in conceptual aircraft design, as conventional empirical laws linking maximum takeoff mass (m_{mto}) to operating empty mass (m_{oe}) do not encompass these novel configurations. Hence, there is a need to employ a more detailed component-based mass estimation approach. In this work, it is assumed that m_{oe} minus wing mass (m_{wing}) and powertrain mass (m_{pt}), denoted as m'_{oe}, remains independent of the powertrain architecture, as proposed by the authors of Ref. [22]. Therefore, m_{oe} can subsequently be determined as the sum of m'_{oe}, m_{pt}, and m_{wing}. The value of m'_{oe} can be determined either by further subdividing the airframe into its major components and applying empirical relations to establish the corresponding masses. Alternatively, in retrofitting scenarios, it may be possible to derive its value for the reference aircraft. For the ONERA Dragon, m'_{oe} is approximated to be 24,900 kg. This value is determined with a m_{oe} of 42.7 t and a m_{pt} of 9.4 t [15].

The estimation of m_{fuel} is obtained by using the Breguet range equation for a cruise-climb scenario, coupled with the definition of

Downloaded from asmedigitalcollection.asme.org/gasturbinespower/article-pdf/148/11/111002/7625683/gtp-25-1623.pdf by Technische Universiteit Delft - Bibliotheek user on 20 October 2026

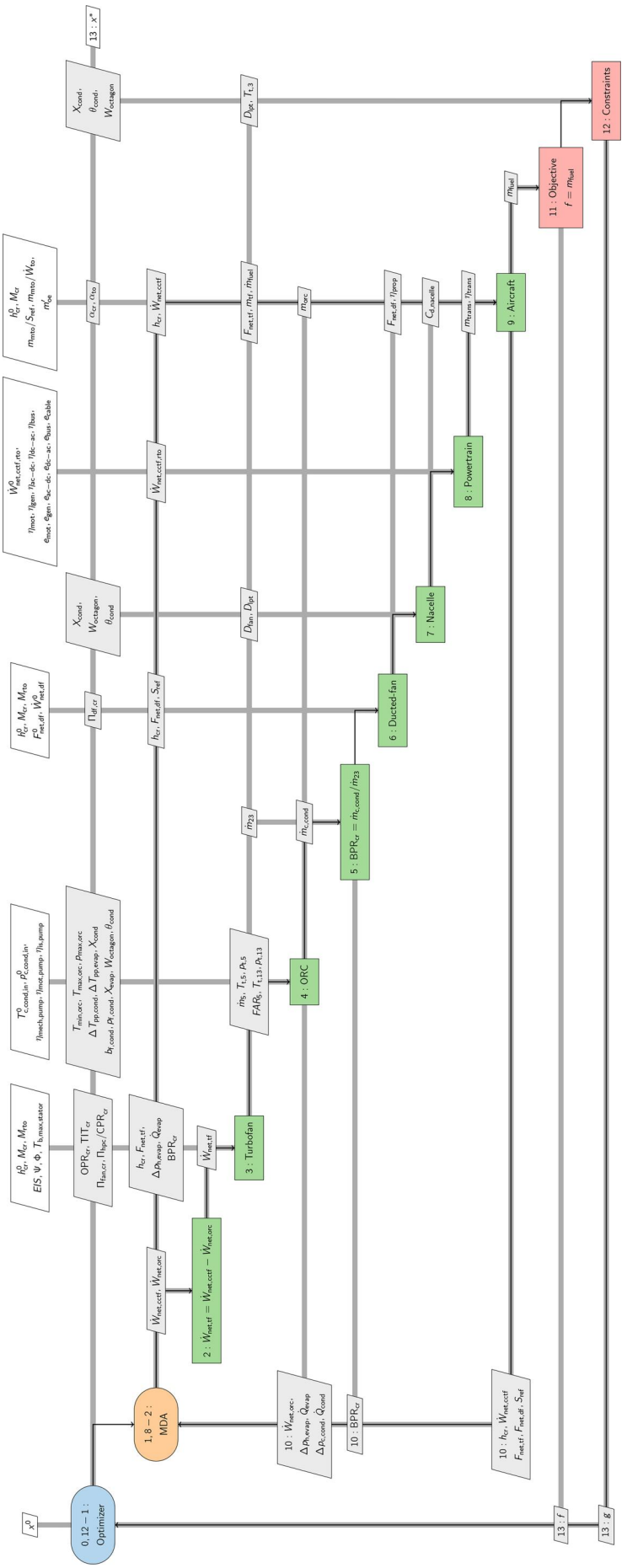


Fig. 4 XDSM of CC-TF aircraft system model

Downloaded from asmedigitalcollection.asme.org/gasturbinespower/article-pdf/148/11/111002/7625683/gtp-25-1623.pdf by Technische Universiteit Delft -Bibliotheek user on 20 October 2026

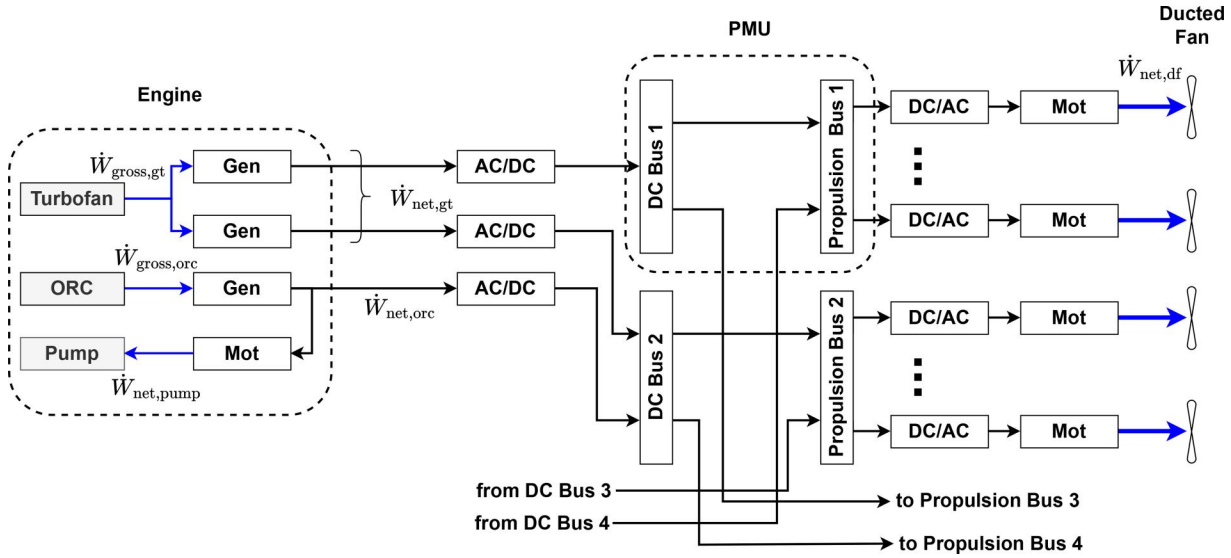


Fig. 5 Flowchart of the powertrain architecture of the partial-turboelectric CC-TF aircraft (adapted from Ref. [15]). Thick blue lines indicate mechanical power transmission, and thick black lines indicate electric power transmission. (Color version online.)

an equivalent cruise range according to the guidelines provided in Ref. [23]. This equivalent cruise range encompasses the nominal cruise range specified by the TLARs, a lost range accounting for fuel consumption during climbing, and additional range factors for divergence, holding, and contingency. Assumptions include a divergence range of 400 km, a holding time of 30 min, and a contingency fraction of 5%. The cruise phase is executed at a constant Mach number, optimizing for the maximum lift-to-drag ratio (L/D), thereby establishing a continuous cruise-climb trajectory.

To ensure that the partial-turboelectric aircraft meets the design requirements set for the ONERA Dragon aircraft, identical wing-loading and power-loading values based on the maximum takeoff mass are employed. The wing-loading is 559 $\mathrm{kg/m^2}$, and the power-loading based on the output power of the electric generators is 2930 kg/MW. Using these values together with the evaluated m_{mto}, the values of required wing area (S_{ref}) and the equivalent generator output power during rolling-takeoff ($\dot{W}_{\mathrm{net,eq,rto}}$) are determined. $\dot{W}_{\mathrm{net,eq,rto}}$ is the generator output power required if the ducted fans produce the full thrust, i.e., for a propulsion system architecture equivalent to that of the original ONERA Dragon aircraft. Subsequently, the equivalent net thrust generated by the ducted fans is calculated according to

$$F_{\mathrm{net,eq,rto}} = \frac{\eta_{\mathrm{prop,df,rto}}\eta_{\mathrm{trans}}\dot{W}_{\mathrm{net,eq,rto}}}{V_{\infty,\mathrm{rto}}} \tag{1}$$

where $\eta_{\mathrm{prop,df,rto}}$ is the propulsive efficiency at RTO, and η_{trans} is the powertrain transmission efficiency defined in Eq. (4).

Assuming that this hypothetical fully turboelectric aircraft and the partial-turboelectric aircraft share the same design except for the propulsion system architecture, the value of $F_{\mathrm{net,eq,rto}}$ is taken as the required thrust at RTO ($F_{\mathrm{req,rto}}$) of the considered partial-turboelectric aircraft. Subsequently, the required thrust at the SLS operating point ($F_{\mathrm{req,sls}}$) is determined based on a thrust lapse rate of $F_{\mathrm{req,rto}}/F_{\mathrm{req,sls}} = 0.8$, which is a suitable value for turbofan engines with a bypass ratio in the range of 5 to 8 at RTO conditions [24].

Once these values are computed, the thrust requirements of the engine and the ducted fans are calculated separately, using relations that are valid for all the considered operating points, namely, CR, RTO, and SLS. The net thrust required by a single engine ($F_{\mathrm{net,eng}}$) and a single ($F_{\mathrm{net,df}}$) are calculated with

$$F_{\mathrm{net,eng}} = \frac{F_{\mathrm{req}}\alpha}{N_{\mathrm{eng}}} \quad \text{and} \quad F_{\mathrm{net,df}} = \frac{F_{\mathrm{req}} - N_{\mathrm{eng}}F_{\mathrm{net,eng}}}{N_{\mathrm{df}}} \tag{2}$$

where N_{eng} and N_{df} are the number of engines and ducted fans, respectively. Furthermore, the words "engine" and subscript "eng" are used to refer to both the simple-cycle turbofan and the CC-TF engine. The thrust ratio (α), the ratio between the net thrust provided by the engines and the total required thrust (F_{req}), is an input for all three operating points. The same value of α is set for both the RTO and SLS operating points.

With $F_{\mathrm{net,df}}$, the required generator output power of a single engine ($\dot{W}_{\mathrm{net,eng}}$) can be evaluated as

$$\dot{W}_{\mathrm{net,eng}} = \frac{N_{\mathrm{df}}F_{\mathrm{net,df}}V_{\infty}}{\eta_{\mathrm{trans}}\eta_{\mathrm{prop,df}}N_{\mathrm{eng}}} \tag{3}$$

where V_{∞} is the freestream velocity, η_{trans} is the powertrain transmission efficiency (Eq. (4)), and $\eta_{\mathrm{prop,df}}$ is the propulsive efficiency at the given operating point. In the case of the simple-cycle turbofan engine, $\dot{W}_{\mathrm{net,eng}}$ equals the net output power of the generators ($\dot{W}_{\mathrm{net,gen}}$). In the case of the CC-TF engine, $\dot{W}_{\mathrm{net,eng}}$ is the sum of $\dot{W}_{\mathrm{net,gen}}$ and the net power output of the ORC unit ($\dot{W}_{\mathrm{net,orc}}$) (see Fig. 5).

The cruise altitude (h_{cr}) is determined based on the cruise Mach number, C_{L}, and the midcruise aircraft mass (m_{cr}). All cruise-related parameters are evaluated based on m_{cr}, which is approximated according to Ref. [23] as $m_{\mathrm{cr}} = \sqrt{m_{\mathrm{mto}}(m_{\mathrm{mto}} - m_{\mathrm{fuel,cr}})}$, where $m_{\mathrm{fuel,cr}}$ is the fuel mass required for the cruise range according to the TLARs.

2.3 Powertrain Architecture. The powertrain architecture of the partial-turboelectric aircraft is similar to that of the ONERA Dragon, differing only in the configuration of the prime mover. However, as only part of the thrust is produced by the distributed propulsion system, the powertrain of the partial-turboelectric aircraft is expected to be lighter as the powertrain can be sized for a lower electrical load. In the following, the words engine and subscript eng are used to refer to both the simple-cycle turbofan and the CC-TF engine.

The main components of the powertrain are the engines, the electrical power transmission components, and the distributed propulsion system consisting of electric motors and ducted fans mounted under the wings. The powertrain comprises two engines ($N_{\mathrm{eng}} = 2$), while the distributed electric propulsion system features 26 ducted fans ($N_{\mathrm{df}} = 26$). Figure 5 shows half of the cross-redundant architecture of the partial-turboelectric aircraft. For simplicity, fault current limiters and circuit breakers are omitted in this flowchart.

Downloaded from asmedigitalcollection.asme.org/gasturbinespower/article-pdf/148/11/111002/7625683/gtp-25-1623.pdf by Technische Universiteit Delft - Bibliotheek user on 20 October 2026

The powertrain mass (m_{pt}) is the sum of twice the engine mass (m_{eng}) and the mass of the electrical power transmission components (m_{trans}). The engine mass is comprised of the gas turbine mass (m_{gt}), the mass of the two gas-turbine-mounted generators (m_{gen}), and, in the case of the CC-TF engine, the mass of the ORC unit assembly (m_{orc}). m_{trans} is the sum of the masses of each electrical component, which are determined by dividing the rated power of each component by its mass-specific power. The powertrain transmission efficiency (η_{trans}) accounts for losses occurring in the electrical components between the engine electric generator and the ducted fans, and it is calculated as

$$\eta_{trans} = \eta_{acdc}\eta_{pmu}\eta_{dcac}\eta_{mot} \tag{4}$$

where η_{acdc} is the rectifier efficiency, η_{pmu} is the combined efficiency of the DC busses, η_{dcac} is the inverter efficiency, and η_{mot} is the electrical motor efficiency. In the case of the CC-TF engine, the combined power output of the generators of the gas turbine ($\dot{W}_{net,gt}$) and of the ORC unit ($\dot{W}_{net,orc}$) equals the required power, which is determined with Eq. (3). The gross shaft power demand of the gas turbine engine ($\dot{W}_{gross,gt}$) is calculated by dividing $\dot{W}_{net,gt}$ by the generator efficiency (η_{gen}). The combined efficiency of the partial-turboelectric propulsion system is defined as

$$\eta_{tot,sys} = \frac{(N_{eng}F_{net,eng} + N_{df}F_{net,df})V_\infty}{N_{eng}\dot{m}_{fuel}\mathrm{LHV}} \tag{5}$$

where $\dot{m}_{fuel}$ is the fuel mass flow rate of a single engine, and LHV is the lower heating value of the fuel, which is 43 MJ/kg for kerosene.

2.3.1 Powertrain Design Assumptions. Table 1 lists mass-specific power and efficiency values for all the electrical components, which are designed for maximum power demand, thus typically for RTO. Values for generator efficiency and mass-specific power are set equal to those of an experimental 4 MW aerospace-grade generator described in Ref. [25]. However, values of mass-specific power and efficiency for the ORC turbogenerator are determined differently, i.e., with the dedicated tool described in Sec. 2.5. These values are given in Table 2. The variation of the size and mass of turbomachinery and nacelle with input power is not modeled, and the variation of the number of ducted fans (N_{df}) with respect to the reference aircraft is not considered. However, the variation of the mass of motors is considered as described in this section. Furthermore, the mass of the thermal management system of the electrical drivetrain is not modeled, and it is considered to be part of m'_{oe} (see Sec. 2.2).

2.4 Engine. The thermodynamic performance of the engine in design and off-design conditions is calculated with the PYTHON library PYCYCLE [27]. Jet-A is considered as the fuel. Similarly to the previous study reported in Ref. [12], turbomachinery polytropic efficiencies are determined using correlations reported in Ref. [28], which are derived from the method described in Ref. [29, Chap. 5]. Based on statistical data, this method estimates turbomachinery efficiency as a function of the entry into service (EIS) year and the stage loading. It also considers scale effects based on the reduced mass flow rate at the entrance of the component.

Table 1 Assumed values of mass-specific power and efficiency of the electric components

Component	Mass-specific power (e) (kW/kg)	Efficiency (η) (%)
Generator (Gen)	17.3	98
Motor (Mot)	19.0	98
Inverter (AC/DC)	19.0	98
Converter (DC/AC)	19.0	98
Power management unit (PMU)	20.0	99
Cables	16.0[a]	100[b]

Values for the generator are taken from Ref. [25]. Values for all other components are taken or estimated from Ref. [15] assuming a moderate technology level.
[a]The value is estimated by dividing the takeoff power by the overall cable mass as given for the ONERA Dragon aircraft in Ref. [26] and is therefore not a generally applicable value.
[b]Losses due to ohmic resistance are neglected for simplicity.

Table 2 Input variables for the specification of the thermodynamic cycle of the ORC system

Parameter	Input	Variable	Input
$T_{max,orc}$	Design variable	$\Delta p_{h,ecap}$	HEX model
$T_{min,orc}$	Design variable	$\Delta p_{c,evap}$	HEX model
$p_{max,orc}$	Design variable	$\Delta T_{pp,evap}$	Design variable
$T_{c,cond,in}$	Ram-duct model	$\Delta p_{h,cond}$	HEX model
$\dot{m}_{h,evap}$	Gas turbine model	$\Delta p_{c,cond}$	HEX model
$T_{h,evap,in}$	Gas turbine model	$\Delta T_{pp,cond}$	Design variable

Note: Subscripts h and c indicate heat exchanger (HEX) hot and cold sides.

The turbine cooling model reported in Ref. [30] is adopted to estimate the cooling air demand as a function of the maximum allowable turbine blade temperature and technology level. Additionally, this model estimates the degradation of turbine efficiency as a function of the cooling flow rate. The maximum allowable rotor blade temperature is estimated assuming creep as the dominant failure mechanism. A method to determine this temperature as a function of blade material, blade stress, and desired minimum lifetime for a certain amount of creep strain is explained in Ref. [11]. The maximum allowable stator blade temperature ($T_{max,stator}$) is set to a constant value. The virtual rotor inlet temperature method of Ref. [31, Part D, Chap. 5] is applied to split the stator and rotor cooling air fractions into *nonchargeable* and *chargeable* cooling flows. The nonchargeable cooling flows are injected before the first turbine rotor and contribute to the work extraction; the chargeable cooling flows are injected at the exit of the turbine and do not contribute to work extraction.

The mass of the gas turbine engine excluding the mass of the electric generators (m_{gt}) is estimated using a correlation valid for geared turbofan engines provided in Ref. [32]. This correlation requires as input the values of the bypass ratio, OPR, and the core mass flow rate at SLS conditions. The mass of the electrical generators is calculated by dividing the takeoff shaft power by the value of the mass-specific power given in Table 1.

An in-house tool for the mechanical design of gas turbine engines coded in PYTHON and named WEST (Refs. [33] and [34]) is used to design the engine gas path. For this purpose, WEST requires as input the thermodynamic conditions, shaft speeds, and turbomachinery duty coefficients at the engine design point, as well as geometrical features such as blade aspect ratios, taper ratios, and connecting duct lengths. Gas path dimensions such as fan diameter (D_{fan}) and engine length (L_{engine}) are used for the sizing of the nacelle and of the air-intake. The air-intake length (L_{intake}) is calculated with a fixed ratio of fan diameter to air-intake length of 0.65 suggested in Ref. [24].

The gas generator efficiency is defined as

$$\eta_{gg} = \frac{0.5\dot{m}_{45}\left(V_{45,id}^2 - V_\infty^2\right)}{\dot{m}_{fuel}\cdot \mathrm{LHV}} \tag{6}$$

where the numerator defines the enthalpy available at the exit of the high-pressure turbine (HPT) (engine station 45) if the exhaust gas was isentropically expanded to ambient conditions reaching the speed $V_{45,id}$. The following definition of propulsive efficiency of the turbofan bypass stream is adopted

$$\eta_{prop,byp} = \frac{F_{net,byp}V_\infty}{\dot{W}_{fan}\frac{\mathrm{BPR}}{1+\mathrm{BPR}}} \tag{7}$$

Downloaded from asmedigitalcollection.asme.org/gasturbinespower/article-pdf/148/11/111002/7625683/gtp-25-1623.pdf by Technische Universiteit Delft - Bibliotheek user on 20 October 2026

Table 3 Engine design assumptions

Parameter	Value	Parameter	Value
$dPqP_{intake}$	0.002 [24, Chap. 4]	$C_{fg,cr}$[a]	97% [21, Chap. 8]
$dPqP_{duct,byp}$	0.01 [29, Chap. 5]	$C_{fg,rto}$[a]	99% [21, Chap. 8]
$dPqP_{duct,exh}$	0.015 [17]	$C_{fg,sls}$[a]	99% [21, Chap. 8]
$dPqP_{noz}$[a]	0.003 [24, Chap. 4]	RTDF	0.13
$dPqP_{cc}$	0.04 [24, Chap. 4]	OTDF	0.3
$\eta_{mech,hp}$	99.6% [24, Chap. 4]	ΔT_{tbc}	100 K
$\eta_{mech,lp}$	99.6% [24, Chap. 4]	$T_{max,stator}$	1755 K
$\eta_{mech,gbx}$	99% [35]		

[a]Same for core and bypass nozzle.

Table 4 Values of duty coefficient assumed for the design of turbomachinery

Parameter	Value	Parameter	Value
Ψ_{fan}	1.0	Φ_{fan}	1.2
Ψ_{lpc}	0.3	Φ_{lpc}	0.7
Ψ_{hpc}	0.3	Φ_{hpc}	0.6
Ψ_{hpt}	1.7	Φ_{hpt}	0.5
Ψ_{lpt}	1.9	Φ_{lpt}	1.0

$F_{net,byp}$ is the net thrust of the bypass stream, and the denominator relates to the fraction of the shaft power transferred to the fan ($\dot{W}_{fan}$) required to compress the bypass air stream. The propulsive efficiency in Eq. (7) is defined in the same way as the propulsive efficiency of the ducted fans (Eq. (19)), which allows a direct performance comparison of both propulsors. For the simple-cycle turbofan engine of the reference aircraft, the bypass ratio during cruise (BPR_{cr}) is given as a design variable. For the CC-TF engine BPR_{cr} is calculated as

$$BPR_{cr} = \frac{\sum \dot{m}_{c,cond}}{\dot{m}_{23}} \tag{8}$$

where the numerator is the condenser cold side air mass flow rate ($\dot{m}_{c,cond}$) summed over all condensers and the denominator is the core air mass flow rate at cruise ($\dot{m}_{23}$). The nozzle gross thrust coefficient (C_{fg}) is a measure of the nozzle efficiency, and it takes into account all the losses due to viscous effects and flow angularity [24]. It is defined as

$$C_{fg} = \frac{F_g}{F_{g,i}} \tag{9}$$

which is the ratio of the actual gross thrust (F_g) to the ideal gross thrust ($F_{g,i}$).

2.4.1 Engine Design Assumptions. Table 3 gives the design assumptions for an EIS year of 2035. The thermodynamic design point of the engine is CR at ISA+15 conditions. The considered off-design points are RTO and SLS. Sea level conditions and a Mach number of 0.25 are set for the RTO operating point. The cooling system is designed at the RTO operating point, and an advanced film cooling technique is assumed (cooling configuration 6 according to Ref. [30, Table 1]). The cooling air mass fractions determined at RTO are set equal at all other operating points. This is common practice for gas turbine performance simulations [36]. For the determination of the turbine cooling flow rate, a maximum allowable stator blade temperature of 1755 K is selected, assuming ceramic matrix composite as the construction material [35]. The single-crystal alloy TMS-238 is chosen as the turbine blade metal, and its characteristics are documented in Ref. [37]. A 100 K temperature difference is assumed across the thermal barrier coating (ΔT_{tbc}) applied to the stator and rotor blades [29]. Furthermore, a radial temperature distribution factor (RTDF) of 0.13 and an overall temperature distribution factor (OTDF) of 0.3 are assumed based on data provided in Ref. [29]. The values adopted for the gross thrust coefficient of the core and bypass nozzles are based on experimental data of 1970s-era turbofan engines presented in Ref. [21]. The values of the relative pressure drop in the exhaust and bypass ducts (dPqP, the variable acronym is taken from Ref. [35]) are fixed and the same for all operating points. In the case of the CC-TF engine, these values serve as the baseline, and the pressure drop due to the heat exchangers is added to the baseline value.

The high-pressure spool speed at the design point is set to 25,000 rpm, which is determined based on mechanical considerations. The rotational speed of the low-pressure spool at the design point is set to the design speed of the electric generators mounted to that shaft, which is 15,000 rpm [25]. The fan speed at the design point is calculated assuming an axial inflow Mach number of 0.6, a fan rotor hub-to-tip ratio of 0.3, and a relative rotor tip Mach number of 1.3. Table 4 reports the turbomachinery work coefficients (Ψ) and flow coefficients (Φ) used for engine sizing and turbomachinery efficiency estimation.

The engine design is less sensitive to the value of the degree of reaction. Therefore, for all turbomachines except for the fan, a value of 0.5 is adopted. For the fan, a value of 0.75 is used, which, for the selected work coefficient, results in zero swirl at the exit of the fan stator vanes.

2.5 Organic Rankine Cycle Unit. For on-design thermodynamic cycle calculations of the ORC unit, an in-house tool written in PYTHON named PYCLE is employed. For the calculation of thermodynamic properties of the working fluid, this tool employs a state-of-the-art Helmholtz equation of state model implemented in the open-source library COOLPROP [38]. The ORC turbine gross power output ($\dot{W}_{gross,orc}$) is converted into electrical power via a dedicated electrical generator (see Fig. 5). An electrical motor drives the ORC pump whose net power input ($\dot{W}_{net,pump}$) is assumed to be provided by the ORC turbogenerator (see Fig. 3). Therefore, the ORC net power output is calculated as

$$\dot{W}_{net,orc} = \dot{W}_{gross,orc}\eta_{mech,turb}\eta_{gen,orc} - \frac{\dot{W}_{net,pump}}{\eta_{mech,pump}\eta_{mot,pump}} \tag{10}$$

taking into account the mechanical efficiency of the ORC turbine ($\eta_{mech,turb}$), the ORC generator efficiency ($\eta_{gen,orc}$), the mechanical efficiency of the pump ($\eta_{mech,pump}$), and the efficiency of the electric motor of the pump ($\eta_{mot,pump}$). The net efficiency of the ORC system is defined as

$$\eta_{net,orc} = \frac{\dot{W}_{net,orc}}{\dot{Q}_{evap}} \tag{11}$$

where $\dot{Q}_{evap}$ is the thermal power recovered by the evaporator of the ORC system.[1] Furthermore, the recovery factor (χ) describes how much of the available thermal power ($\dot{Q}_{exh,avail}$) is recovered by the WHR system, and it is defined as

$$\chi = \frac{\dot{Q}_{evap}}{\dot{Q}_{exh,avail}} \tag{12}$$

$\dot{Q}_{exh,avail}$ is defined as the product of the exhaust gas mass flow rate and the specific enthalpy difference between the state of the exhaust gas at the turbine exit and that at ambient conditions.

The ORC system mass (m_{orc}) is the sum of the turbogenerator mass (m_{tg}), the pump mass (m_{pump}), the mass of all condensers ($\sum m_{cond}$), the evaporator mass (m_{evap}), the working fluid mass (m_{fluid}), and the balance-of-plant mass ($m_{bop,orc}$). The heat exchanger

[1]This heat exchanger is called evaporator even if, being the fluid supercritical, no phase change takes place. However, the fluid at the exit is in a vapor-like state, and an evaporator is often used also in the case of supercritical power plants. Alternatively, this heat exchanger is also called primary heat exchanger.

Downloaded from asmedigitalcollection.asme.org/gasturbinespower/article-pdf/148/11/111002/7625683/gtp-25-1623.pdf by Technische Universiteit Delft - Bibliotheek user on 20 October 2026

and turbogenerator masses are outputs of the respective design routine. m_{fluid} is estimated as the product of 1.2 times the evaporator cold side volume and the density of the working fluid at one atmosphere and 25 °C. Additionally, it is assumed that $m_{bop,orc}$ constitutes 10% of m_{orc}. This value is comparable to that assumed in Ref. [7]. Nevertheless, the mass assumed for the balance-of-plant components is uncertain due to the limited knowledge available on the design of ORC systems for airborne applications. The BoP comprises the piping and all components required for ORC unit operation, such as the condensate vessel to accommodate variations in the working fluid mass within the circuit under different operating conditions and a bypass line to facilitate the startup of the working fluid loop.

2.5.1 Organic Rankine Cycle Unit Design Assumptions. Figure 3 shows the process flow diagram of the CC-TF engine and, with it, that of the ORC unit, which is of an air-cooled nonrecuperated configuration. A supercritical thermodynamic cycle is adopted. The rationale for this choice is to improve temperature profile matching between the working fluid and the exhaust gases in the evaporator, thereby reducing exergy destruction and maximizing the thermal efficiency of the ORC system. As explained in Ref. [11], in the particular case of an airborne system, aircraft fuel efficiency benefits more from maximizing the ORC unit thermal efficiency than from recovering more thermal energy, which significantly impacts component weight. This suggests that a recuperated ORC configuration could be preferable to the simple-cycle one. Furthermore, the adoption of a recuperator may allow a reduction in condenser and evaporator size. However, preliminary calculations led to discarding the recuperated configuration due to the added weight of the recuperator and a reduced pinch point temperature difference in the evaporator caused by a higher working fluid inlet temperature. However, further investigations are needed and will be addressed in future work together with the assessment of different working fluids.

Improvements in fuel efficiency over the cruise phase have the largest impact on the overall mission fuel consumption. Therefore, the thermodynamic design point of the ORC WHR unit is the same as that of the prime mover, i.e., CR at ISA+15 conditions. It is assumed that the ORC unit is not operational in operating conditions other than CR. The reason is that the current implementation of the design tool PYCLE is limited to on-design simulations only. Therefore, the effect of the pressure drop caused by heat exchangers and the variation of heat transfer rate on gas turbine performance, and the contribution of the ORC system to power production are not evaluated at these operating points. It is hypothesized that the ORC condenser heats the bypass stream just enough to balance the negative effect of aerodynamic drag due to the presence of the heat exchanger in the bypass. The validity of this hypothesis is confirmed by the results of engine off-design simulations if it is assumed that the pressure drop and heat transfer to the bypass stream caused by the condenser are the same as in cruise conditions. At the same time, the influence of neglecting the contribution of the ORC system to the overall performance at operating points other than cruise is minimal because:

(1) The relatively high ambient temperature at sea level implies that the condensation temperature of the working fluid is much higher than during cruise operation; thus, the value of $\eta_{net,orc}$ is considerably lower.
(2) At takeoff, the heat capacity (mass flow rate times specific heat capacity) in the core and bypass streams of the gas turbine is appreciably larger than during cruise. However, the heat exchangers of the ORC system are designed for thermal loads during cruise. Therefore, the evaporator cannot exploit the large amount of thermal power discharged by the gas turbine at takeoff. In addition, the bypass air temperature increase due to the thermal power discharged by the ORC condenser is small due to the large air mass flow rate at takeoff; therefore, its positive effect on propulsive efficiency is expected to be small.

Cyclopentane is assumed as the working fluid of the ORC unit. Cyclopentane is characterized by a critical temperature (T_{crit}) of 512 K, a critical pressure (p_{crit}) of 4.51 MPa, and a normal boiling point temperature of 322 K [39]. As discussed in Ref. [40], cyclopentane is a suitable working fluid for ORC systems recovering thermal energy from gas turbine engines of stationary power plants and is adopted for power plants in operation.[2] Favorable characteristics are its high thermal stability in contact with stainless steel ($T_{max,fluid}$) of 573 K [41] and high T_{crit}. Cyclopentane suitability for the analyzed application is supported by a study investigating the impact of working fluid selection on the performance of airborne ORC WHR systems. Among the analyzed hydrocarbons, the results indicate that cyclopentane yields the best overall performance in terms of fuel mass savings [42].

Regarding the safety hazards associated with the adoption of a flammable fluid such as cyclopentane as the working fluid, which may come into contact with the engine exhaust gases, it should be noted that the likelihood of a fire in the evaporator due to a leak of cyclopentane is low. The exhaust gases are rapidly cooled below the auto-ignition temperature of cyclopentane (634 K), and the residence time of the leaked fluid in the engine is estimated to be much shorter ($(Z_{evap}/u_{avg,exh,HX}) + 1.5\,(X_{evap}/u_{avg,exh,nozzle}) \approx 0.02$ s) than the ignition delay time experimentally observed for air–cyclopentane mixtures (> 0.6 s) [43]. At the same time, special measures may be required to ensure system safety and thus enable engine certification. These may include integrating hydrocarbon leak sensors, coating stainless steel surfaces to prevent catalytic effects that promote combustion, and implementing control strategies that rapidly depressurize the cyclopentane loop and isolate the evaporator in the event of a leak. However, despite these preliminary positive findings, it is possible that cyclopentane is not the optimal fluid for the type of aircraft engines considered in this study, due to both reasons related to system safety and the thermodynamic performance of the resulting combined engine. Other working fluids will be assessed as part of the continuation of this research program.

Concerning the modeling of the ORC turbogenerator, the values of ORC turbine efficiency ($\eta_{is,turb}$) and mass-specific power (e_{tg}) assumed in the study are based on the optimized turbogenerator design obtained with an in-house tool for the CC-TS engine configuration analyzed in Ref. [12]. The turbine efficiency is 95%, which represents an upper limit for typical ORC applications and arises from a combination of moderate pressure ratio and volumetric flow rate per unit of turbine specific work for a radial-inflow turboexpander. Given the possible uncertainty associated with this modeling assumption, the ORC turbine efficiency has been included among the variables of the sensitivity study performed around the optimal CC-TF design solution, whose results are reported in Sec. 3.3. The mass of the turbogenerator is calculated by dividing the turbogenerator net power output by the turbogenerator mass-specific power. The values of the pump isentropic efficiency and the mass-specific power are taken from the work reported in Ref. [44], which documents research on electrically driven centrifugal pumps for small space launch vehicles operating under similar conditions as expected for the pump of the ORC unit. Table 2 summarizes the input variables for the specification of the thermodynamic cycle of the ORC unit and whether they are a design variable or taken from other submodules. Table 5 lists assumed values of efficiencies and mass-specific power of the pump and the turbogenerator.

2.6 Nacelle Model. The nacelle houses all the components of the engine and is connected to the tail cone of the fuselage via a pylon. The drag of the nacelle is estimated based on a simplified geometry that consists of a cylindrical part and a tail cone as

[2]To the author's knowledge, the combined-cycle power plant being built at the Dahshour gas compression station in Egypt, see https://www.turboden.com/solutions/2603/combined-cycles, is an example.

Downloaded from asmedigitalcollection.asme.org/gasturbinespower/article-pdf/148/11/111002/7625683/gtp-25-1623.pdf by Technische Universiteit Delft - Bibliotheek user on 20 October 2026

Table 5 Values of assumed efficiencies and mass-specific power of components of the ORC system

Parameter	Value	Parameter	Value
$\eta_{is,pump}$	65% [44]	$\eta_{mech,turb}$	99% [12]
$\eta_{mot,pump}$	98% [15]	$\eta_{gen,orc}$	97% [12]
$\eta_{mech,pump}$	99%	e_{pump}	4 kW/kg [44]
$\eta_{is,turb}$	95% [12]	e_{tg}	4.5 kW/kg [12]

indicated with a dashed thick line in Fig. 2. The diameter of the nacelle ($D_{nacelle}$) is determined as

$$D_{nacelle} = \max(D_{fan}, W_{octagon} + X_{cond}\cos\theta_{cond}) \tag{13}$$

where D_{fan} is the engine fan diameter, $W_{octagon}$ is the width of the octagon along which the condensers are arranged, X_{cond} is the condenser length, and θ_{cond} is the condenser tilt angle. With reference to Fig. 2, the length of the cylindrical part of the nacelle ($L_{nacelle}$) is the sum of L_{intake}, L_{engine}, the core exhaust duct length (L_{exh}), and the evaporator length (X_{evap}). The value of L_{exh} is set to 0.3 m. The simple-cycle turbofan engine does not incorporate an evaporator, but for the sake of obtaining an approximation of the nacelle size, it is assumed that $X_{evap} = 0.7$ m. This value results from measured values of a cutaway drawing of the Pratt & Whitney PT6 turboshaft engine [19], which adopts a similar exhaust configuration and features an exhaust duct that is approximately 1.1 times longer than the turbine outer diameter. Test calculations related to the design of the CC-TF engine showed that the LPT exit diameter is in the range of 0.6 m. The length of the tail cone (L_{cone}) is fixed to 0.75 m, and its diameter (D_{cone}) is set to the outer diameter of the evaporator. The value of L_{cone} is determined to ensure that there is enough space to place the engine-mounted generators and the ORC turbogenerator. The nacelle drag coefficient ($C_{d,nacelle}$) is estimated based on the flat plate analogy as

$$C_{d,nacelle}S_{ref} = C_{f,turb}(1+\phi)S_{wet,nacelle} \tag{14}$$

where $C_{f,turb}$ is the turbulent flat plate skin friction coefficient and ϕ a factor considering the lift-independent pressure drag contribution. $C_{f,turb}$ is determined with the correlation [20]

$$C_{f,turb} = 0.044/\mathrm{Re}_{co}^{1/6} \tag{15}$$

together with the cutoff Reynolds number (Re_{co}) that is evaluated as [21]

$$\mathrm{Re}_{co} = 36.82 * (L_{nacelle}/h_{eq,sand})^{1.072} \tag{16}$$

using an equivalent sand grain roughness ($h_{eq,sand}$) value of 0.001 in. The width of the pylon is taken to be 25% of $D_{nacelle}$, a value which lies in the range suggested in Ref. [45], and its length is set equal to $L_{nacelle}$. The drag caused by the pylon is estimated using Eq. (14), with the same values of $C_{f,turb}$ and ϕ adopted for the calculation of the nacelle drag. Additionally, an interference drag amounting to 10% of the combined nacelle and pylon drag is assumed, as suggested in Ref. [45]. The mass of the nacelle is considered part of m'_{oe}, and its variation with nacelle size is not accounted for.

2.7 Model. The on-design and off-design thermodynamic performance of ducted fans mounted under the wings is calculated with the PYTHON library PYCYCLE [27]. An assembly consists of an air-intake, a fan driven by an electric motor, a duct, and a variable-area nozzle. A variable-area nozzle is employed to improve propulsive efficiency during takeoff and to prevent the surge of the fan. For simplicity, a conical nozzle is assumed, although it is acknowledged that a square-shaped nozzle would be more practical for adapting the throat area. The surge margin at a constant reduced mass flow rate (SM_m) is defined as

$$SM_m = \frac{\Pi_{surge} - \Pi_{df}}{\Pi_{df}} \tag{17}$$

where Π_{surge} is the surge pressure ratio at a given reduced mass flow rate, and Π_{df} is the pressure ratio. The polytropic efficiency of the fan is estimated as a function of Π_{df} using the relation reported in Ref. [46] as

$$\eta_{poly,df} = 0.98 - 0.08(\Pi_{df} - 1) \tag{18}$$

The propulsive efficiency of the ducted fans is defined as

$$\eta_{prop,df} = \frac{F_{net,df}V_\infty}{\dot{W}_{net,df}} \tag{19}$$

2.7.1 Design Assumptions. The thermodynamic design point of the ducted fans is CR at ISA+15 conditions. The considered off-design points are RTO and SLS. Sea level conditions and a Mach number of 0.25 are set for the RTO operating point. The same fan map as that assumed for the NASA N+3 engine concept [35] is used, as no better alternative was found in the literature. However, the map of an optimized fan for the studied cases is likely to be different. The variable area nozzle is controlled to ensure a surge margin of 30% at the SLS and RTO operating points. The fan speed at the design point is set to 10,000 rpm, which, for the expected flow conditions during cruise and an assumed hub-to-tip ratio of 0.3, ensures a subsonic tip Mach number. In accordance with data provided in Ref. [24] for component efficiencies of engines with EIS year 2035, for all operating points, relative total pressure losses amounting to 1% for the air-intake, 0.5% for the duct, and 0.3% for the nozzle are assumed. The same values of C_{fg} as for the engine nozzles are applied at the CR, RTO, and SLS operating points (see Table 3). A discussion of the sensitivity of system performance to the value of C_{fg} is presented in Sec. 3.3. The mass of the ducted fans is considered part of m'_{oe}, and the variation of size, nacelle drag, and mass with thrust is not accounted for. Furthermore, the number of ducted fans is kept constant. The variation of electric motor mass with power is considered as part of the powertrain sizing as explained in Sec. 2.3.

2.8 Heat Exchangers. The in-house software HEXACODE, coded in PYTHON, is used for heat exchanger sizing [47]. The validity of this software was confirmed through a comprehensive comparison of results with those of a commercial heat exchanger design and rating code [48]. The sizing process involves determining the necessary heat transfer area for a specified heat duty, considering the inlet temperature, pressure, and mass flow rate of both the hot and cold streams. The program outputs key parameters such as heat exchanger dimensions, mass, and hot and cold side pressure drops. For both the evaporator and condenser, the frontal area is specified, while the depth is computed to satisfy the design requirements. The additional pressure loss associated with the heat exchanger tilt is modeled based on a correlation fitted to experimental results [49].

2.8.1 Heat Exchanger Design Assumptions. The evaporator features an annular arrangement and is designed as a multipass inline bare-tube bundle heat exchanger, with the working fluid flowing inside the tubes in a counter-crossflow arrangement with reference to the exhaust gases (see Fig. 6). The tubes of the evaporator are aligned with the engine axis (see Fig. 2). The nickel-base Hastelloy X® alloy is selected as the construction material, owing to its good oxidation resistance, manufacturability, and strength at high temperatures [29, Chap. 5]. The tube outer diameter is fixed to 1.8 mm, and the tube thickness is computed based on the pressure difference between the exhaust gases and the working fluid. As described in the previous work of the authors [11,12], the engine optimization leads to evaporator designs whereby the air-side pressure drop is minimized. Based on those results, the nondimensional transversal pitch ($x_{t,evap}$) is set to 3.0, the nondimensional longitudinal pitch ($x_{l,evap}$) to 1.25, and the number of passes

Downloaded from asmedigitalcollection.asme.org/gasturbinespower/article-pdf/148/11/111002/7625683/gtp-25-1623.pdf by Technische Universiteit Delft - Bibliotheek user on 20 October 2026

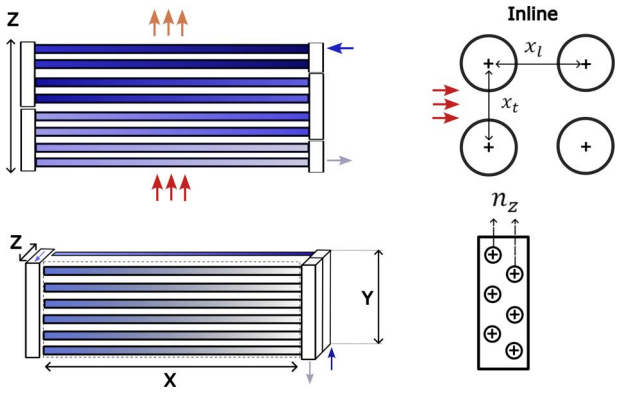


Fig. 6 Geometry of the core of the evaporator: multipass inline bare tube bundle

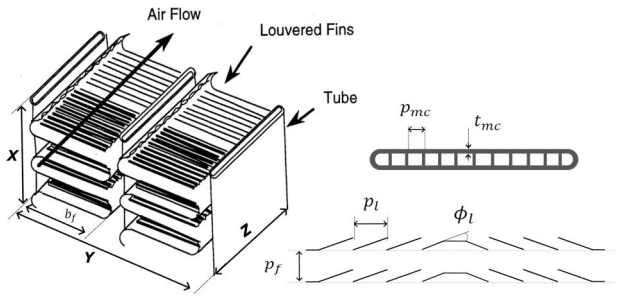


Fig. 7 Geometry of the core of the condenser: flat-tube microchannels with louvered fins

($n_{\text{pass,evap}}$) to 6. The suitability of these values was confirmed to be optimal by additional computational tests for the specific engine configuration considered in the work at hand. The evaporator length (X_{evap}) is an optimization variable. The inner diameter of the annular evaporator equals the LPT outer diameter, and the resulting perimeter is set as the evaporator width (Y_{evap}). The flow distribution of the exhaust gas entering the evaporator perpendicular to the bare tubes is assumed to be uniform for simplicity. Therefore, it can be expected that the resulting pressure drop is underestimated, while the heat transfer rate is overestimated.

The condenser topology is that of a flat-tube microchannel heat exchanger with louvered fins (see Fig. 7). The value of the following design parameters is fixed, based on manufacturability considerations: the flat-tube thickness is 0.2 mm, the fin thickness is 0.11 mm, and the height of the microchannels is 1.6 mm. Additionally, the length of the louver fins and the pitch are both set to be 90% of the fin height and the fin pitch, respectively, based on compact HEX design guidelines reported in Ref. [47]. The louver angle ($\phi_{\text{l,cond}}$) is fixed to 30 deg. The length of the flat-tubes (X_{cond}), the fin height ($b_{\text{f,cond}}$), the fin pitch ($p_{\text{f,cond}}$), and the condenser tilt angle (θ_{cond}) are optimization variables of the condenser. θ_{cond} is the angle between the flat-tubes and the radial direction (see Fig. 2). The width of the condenser (Y_{cond}) is determined by the length of the side of the octagon along which the condensers are arranged. As suggested in a technical report, an aluminum alloy of the 3000 series is selected as the construction material [50].

2.9 System Design Optimization. Numerical optimization is used to identify optimized designs of both the reference aircraft and the CC-TF aircraft that minimize mission fuel mass (m_{fuel}). The constrained, single-objective optimization problem is expressed in mathematical terms as

$$\begin{aligned} \text{minimize} \quad & F(\boldsymbol{x}) = m_{\text{fuel}}(\boldsymbol{x}) \\ \text{subject to :} \quad & x_{\text{i}}^{L} \le x_{\text{i}} \le x_{\text{i}}^{U} \\ & g1 : T_{\text{t,3,rto}} \le 950\,\text{K} \\ & g2 : W_{\text{octagon}} \ge D_{\text{lpt}} + X_{\text{cond}} \cos(\theta_{\text{cond}}) \\ & g3 : X_{\text{cond}} \sin(\theta_{\text{cond}}) \le 1.5\,\text{m} \\ & g4 : \dot{W}_{\text{net,rto}} \ge \dot{W}_{\text{net,cr}} \quad \text{or} \quad \dot{W}_{\text{net,cctf,cr}} \end{aligned} \tag{20}$$

Constraint $g1$ limits the exit temperature of the high-pressure compressor (HPC) at RTO to a mechanically feasible value, which according to Ref. [29, Chap. 5] can be assumed as 950 K. Constraint $g2$ ensures that the condensers are placed outside the physical boundary of the gas turbine core, which is defined by the LPT outer diameter (D_{lpt}) (see Fig. 2). Constraint $g3$ limits the axial extension of the condenser ($X_{\text{cond}} \sin(\theta_{\text{cond}})$) to 1.5 m so that it fits inside the bypass duct of the engine (see Fig. 2). Constraint $g4$ ensures that the electrical powertrain is sized for sufficient power at the RTO point to fulfill the power requirement during cruise.

The design variables x_i together with their lower bounds (x_i^{L}) and upper bounds (x_i^{U}) are listed in Table 6. For the reference aircraft, the design vector ($\boldsymbol{x}$) comprises eight variables related to the aircraft and

Table 6 Design variables and corresponding bounds used to identify optimal designs of the reference aircraft and the CC-TF aircraft designs

Model	Variables (x_{i})	Description (unit)	Bounds (x_i^L/x_i^U)
Aircraft	α_{cr}	Turbofan to total thrust ratio at cruise	0.3/0.6
	α_{to}	Turbofan to total thrust ratio at SLS/RTO	0.3/0.6
Turbofan	OPR_{cr}	Overall pressure ratio	35/60
	TIT_{cr}	Turbine inlet temperature (K)	1500/1800
	$\Pi_{\text{fan,cr}}$	Fan pressure ratio	1.2/1.7
	$(\Pi_{\text{hpc}}/\text{CPR})_{\text{cr}}$	Ratio of HPC to core pressure ratio	0.1/0.3
	BPR_{cr}	Bypass ratio during cruise	4/10
	$\Pi_{\text{df,cr}}$	Fan pressure ratio	1.2/1.5
ORC	$T_{\text{min,orc}}$	Minimum cycle temperature (K)	323/423
	$T_{\text{max,orc}}$	Maximum cycle temperature (K)	520/570
	$p_{\text{max,orc}}$	Maximum cycle pressure (Pa)	$1.1p_{\text{crit}}/1.5p_{\text{crit}}$
	$\Delta T_{\text{pp,cond}}$	Condenser pinch point temperature difference (K)	20/100
	$\Delta T_{\text{pp,evap}}$	Evaporator pinch point temperature difference (K)	20/100
ORC HEX	X_{cond}	Condenser flat-tube length (m)	1.0/2.0
	$b_{\text{f,cond}}$	Condenser fin height (mm)	7.0/16.0
	$p_{\text{f,cond}}$	Condenser fin pitch (mm)	1.0/4.0
	X_{evap}	Evaporator length (m)	0.75/1.5
	W_{octagon}	Width of octagonal condenser arrangement (m)	0.8/2.3
	θ_{cond}	Condenser tilt angle (deg)	50/75

Downloaded from asmedigitalcollection.asme.org/gasturbinespower/article-pdf/148/11/111002/7625683/gtp-25-1623.pdf by Technische Universiteit Delft - Bibliotheek user on 20 October 2026

Table 7 TLARs of the ONERA Dragon [15]

Parameter	Input
Range (NM/km)	2750/5100
Number of passengers	150
Mach number	0.78
Design payload (kg)	13,600

Table 8 Design vector characterizing the optimized reference aircraft

Parameter	α_{cr}	α_{to}	OPR_{cr}	TIT_{cr}	$\Pi_{fan,cr}$	BPR_{cr}	$\Pi_{df,cr}$
Value	0.74	0.85	49.1	1500 K	1.49	8.28	1.39

the thermodynamic cycle of the simple-cycle turbofan engine and the. The design vector of the CC-TF aircraft includes seven of these variables, except for the engine bypass ratio at cruise (BPR_{cr}), which is calculated according to Eq. (8). Additionally, the design vector of the CC-TF includes 11 variables related to the thermodynamic cycle of the ORC and its heat exchangers. The optimization problem is solved using a genetic algorithm implemented in the PYTHON library PYMOO [51]. A population size of at least ten times the number of design variables is used. Convergence is considered achieved if the relative change between the last and the fifth to last generation is below 10^{-6}.

2.10 Framework Verification. The verification of the ARENA framework is presented in Ref. [12], where it is shown that this software suite can reproduce major parameters such as masses and power demand with respect to a turboelectric reference aircraft with an accuracy of ±3%. This is considered sufficiently accurate for the preliminary analysis described here.

3 Results and Discussion

The ARENA framework is used to optimize the preliminary design and to compute the performance of two partial-turboelectric aircraft, whose main characteristics and mission are described in Sec. 2. These aircraft are (1) the reference aircraft propelled by simple-cycle turbofan engines and (2) the CC-TF aircraft powered by CC-TF engines. Both aircraft adopt the same powertrain architecture depicted in Fig. 5 and TLARs listed in Table 7. The design solutions are presented in Secs. 3.1 and 3.2, while the results of the sensitivity study around the CC-TF solution are reported in Sec. 3.3.

Furthermore, in Sec. 3.4, the performance of the CC-TF engine is compared with that of the CC-TS powertrain configuration presented in Ref. [12], given the similarity of the two engine concepts and thereby highlighting the specific advantages of the CC-TF configuration. In Sec. 3.5, a comparison is also made with the NASA N+3 turbofan engine [35], which serves as a representative benchmark for conventional propulsion systems envisaged for entry-into-service aircraft in the 2030–2040 timeframe.

3.1 Optimized Reference Aircraft. The design variables that are optimal in terms of minimum mission fuel consumption result from a tradeoff between propulsion system efficiency and aircraft mass. The optimized design vector of the reference aircraft is given in Table 8, and a summary of the main parameters characterizing the airframe-level and engine-level results is shown in the left columns of Tables 9 and 10, respectively. Detailed data of the reference engine thermodynamic cycle at the CR, RTO, and SLS operating points is provided in Appendix A.

The reference aircraft has a m_{mto} of 63.1 t, a m_{oe} of 36.7 t, and a mission fuel consumption of 12.9 t. The propulsion system has an overall efficiency ($\eta_{tot,sys,cr}$) of 38.6% and a cruise thrust-specific fuel consumption ($TSFC_{cr}$) of 14.4 mg/N·s. The engine mass is determined at the SLS (see Sec. 2.4) and the electrical powertrain mass at the RTO (see Sec. 2.3) operating points. Engine and electrical powertrain mass are a function of takeoff thrust and therefore directly related to the value of α_{to}. To achieve a given turbofan thrust, TIT_{rto} needs to be set accordingly, which in turn affects the required cooling air mass fraction ($m_{frac,cool}$). The cooling air mass fraction is determined based on RTO conditions and set equal at all other operating points. In this way, α_{to} influences the optimal values of the design variables defined at cruise. Propulsion system efficiency during takeoff does not influence mission fuel consumption as explained in Sec. 2.2. The low mass-specific power of the electrical powertrain components is the cause of the large thrust contribution of the turbofan engines during cruise and takeoff. Despite similar values of $\eta_{prop,byp,cr}$ and $\eta_{prop,df,cr}$, the turbofan engines provide 74% of the required cruise thrust. Similarly, at takeoff, the turbofan engines provide 85% of the required thrust, despite $\eta_{prop,df,rto}$ being higher than $\eta_{prop,byp,rto}$. The optimization leads to an electrical powertrain whose design power capacity at takeoff ($\dot{W}_{net,rto}$) is equal to the power requirement during cruise ($\dot{W}_{net,cr}$), thus reaching the limit prescribed by the optimization constraint $g4$ (see Eq. (20)). The values of $\dot{W}_{net,cr}$ and $\dot{W}_{net,rto}$ are determined based on the values of α_{cr} and α_{to}. The optimized design

Table 9 Main parameters characterizing the optimized design of the reference and the CC-TF aircraft

Parameter	Reference aircraft	CC-TF aircraft	Δ%
m_{mto} (t)	63.1	64.2	1.7%
m_{oe} (t)	36.7	38.1	3.8%
m_{pt} (t)	4.10	5.39	31%
m_{wing} (t)	7.66	7.85	2.5%
m_{fuel} (t)	12.9	12.4	−3.9%
m_{eng} (t)	1.62	1.83	13.0%
L/D	16.9	16.9	0.0%
S_{ref} (m^2)	113	115	1.8%
b (m)	34.8	35.1	0.9%
$F_{req,cr}$ (kN)	32.8	33.9	3.4%
$F_{req,rto}$ (kN)	131	130	−0.8%
$F_{req,sls}$ (kN)	163	163	0.0%
$TSFC_{cr}$ (mg/N·s)	14.4	13.5	−6.3%
$D_{nacelle}$ (m)	1.42	1.65	16.2%
$L_{nacelle}$ (m)	4.21	3.80	−9.7%
L_{engine} (m)	1.54	1.21	−21.4%
L_{intake} (m)	0.93	0.75	−19.4%
D_{fan} (m)	1.42	1.16	−18.3%

Table 10 Main parameters characterizing the optimized design of the propulsion system of the reference and the CC-TF aircraft

Parameter	Reference engine	CC-TF engine	Δ%
$\dot{W}_{net,cr}$ (MW)	1.61	2.66	66%
$\dot{W}_{net,rto}$ (MW)	1.61	3.29	105%
OPR_{cr}	49.1	42.2	−14%
$\Pi_{fan,cr}$	1.49	1.64	10%
BPR_{cr}	8.28	7.82	−5.6%
TIT_{cr} (K)	1500	1770	18%
TIT_{rto} (K)	1610	1970	22%
$m_{frac,cool}$	3.3%	8.8%	167%
$\dot{m}_{2,cr}$ (kg/s)	119	76	−36%
ST_{cr} (N/kg/s)	100	130	30%
$dPqP_{byp,cr}$	1.0%	2.8%	180%
$dPqP_{exh,cr}$	1.5%	5.0%	233%
$\eta_{prop,byp,cr}$	70.0%	78.9%	13%
$\eta_{prop,byp,rto}$	45.6%	40.9%	−10%
$\Pi_{fan,df,cr}$	1.39	1.37	−1.4%
$\eta_{prop,df,cr}$	69.4%	69.7%	0.4%
$\eta_{prop,df,rto}$	56.8%	55.6%	−2.1%
$\eta_{tot,sys,cr}$	38.6%	41.3%	7.0%

Downloaded from asmedigitalcollection.asme.org/gasturbinespower/article-pdf/148/11/111002/7625683/gtp-25-1623.pdf by Technische Universiteit Delft - Bibliotheek user on 20 October 2026

Table 11 Design vector characterizing the optimized CC-TF engine

Parameter	α_{cr}	α_{to}	OPR_{cr}	TIT_{cr}	$\Pi_{fan,cr}$	$\Pi_{df,cr}$	$T_{min,orc}$	$T_{max,orc}$	$p_{max,orc}$
Value	0.58	0.70	42.2	1770 K	1.64	1.37	361 K	551 K	59.5 bar
Parameter	$\Delta T_{pp,cond}$	$\Delta T_{pp,evap}$	X_{cond}	$b_{f,cond}$	$p_{f,cond}$	X_{evap}	$W_{octagon}$	θ_{cond}	
Value	29 K	86 K	1.56 m	12 mm	3 mm	0.78 m	1.11 m	74 deg	

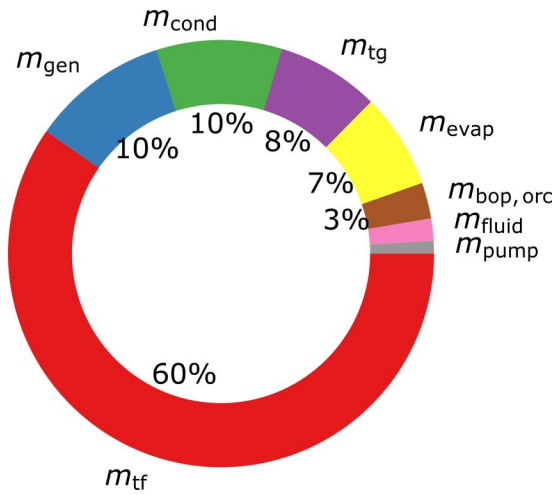


Fig. 8 Mass breakdown of the components of the CC-TF engine. The mass of the electrical generators m_{gen} and the condensers m_{cond} are the sums of the masses of two and eight units, respectively.

selects a value of α_{cr} that results in minimum fuel consumption. Since $\dot{W}_{net,cr} = \dot{W}_{net,rto}$, the performance of the distributed propulsion system at the cruise operating point determines the value of α_{to}.

3.2 Optimized Combined-Cycle Turbofan Aircraft. The optimal preliminary design of the CC-TF engine is the result of a highly complex tradeoff between thermodynamic performance, mass of all the components, and its effect on aircraft aerodynamics. This tradeoff is made evident by the values of the optimized design vector of the CC-TF aircraft listed in Table 11. The pie chart of Fig. 8 shows the mass breakdown of the components of the CC-TF engine. Furthermore, Tables 9 and 10 list all the main parameters defining the preliminary design of the engines and the aircraft of both the reference and the CC-TF aircraft for comparison. Detailed data of the CC-TF engine thermodynamic cycle at the CR, RTO, and SLS operating points is provided in Appendix B.

The adoption of the ORC WHR system reduces the $TSFC_{cr}$ of the CC-TF aircraft during cruise by 6.3% and m_{fuel} by 3.9% if compared to the reference aircraft. The overall propulsion system efficiency at cruise conditions ($\eta_{tot,sys,cr}$) increases by 7%.

Compared to the simple-cycle turbofan engine, the optimal CC-TF engine is characterized by smaller values of BPR_{cr} and OPR_{cr}, and higher values of TIT_{cr} and $\Pi_{fan,cr}$. In general, the efficiency of combined-cycle engines benefits from higher TIT if compared to a simple-cycle engine featuring the same OPR [36]. Therefore, the optimized engine is characterized by a value of TIT_{cr} higher than that of the simple-cycle turbofan engine. The bypass ratio of the CC-TF engine is determined with Eq. (8) and is therefore a function of the mass flow rate of air flowing through the condenser, which is an outcome of the simulation of the ORC system operating at design conditions. The ORC system design depends on limitations constraining the size of the condenser, the effect of the size of the condenser on nacelle drag, and the impact of the pressure drop over the condenser airflow on engine thrust.

The optimization leads to the highest possible condenser tilt angle to reduce $D_{nacelle}$ (see Eq. (13)). In combination with this angle and to maximize heat transfer area, the optimal condenser length is the maximum possible set by constraint $g3$ of Eq. (20). The value of the $W_{octagon}$ design variable is a result of the tradeoff between the increase in BPR_{cr} and nacelle drag.

Table 12 summarizes all the main parameters resulting from the design optimization of the ORC unit and obtained concurrently with the optimization of the turbofan engine. Figure 9 displays the processes of the thermodynamic cycles of the gas turbine and ORC system on the temperature–entropy diagram, and Fig. 10 shows the temperature–heat load diagrams of the evaporator and the condenser. The calculated net thermal efficiency of the ORC system is 17.7%. The minimum cycle temperature is 361 K, and the maximum cycle temperature is 551 K, which is close to the specified temperature limit related to the thermal stability threshold of the working fluid (see Sec. 2.5). The maximum working fluid pressure in the evaporator is 59.5 bar, while the minimum working fluid pressure in the condenser is 3.1 bar. Thus, no inward air leaking into the working fluid loop is possible. Further analysis shows that the ORC system is optimized for maximum thermal efficiency rather than maximum thermal power input. This is in contrast to the design of stationary ORC systems recovering thermal power from industrial gas turbines, which are designed to recover the maximum

Table 12 Relevant design specifications of the optimized ORC WHR system at cruise

Parameter	Value	Parameter	Value	Parameter	Value
$\eta_{net,orc}$	17.7%	$\dot{Q}_{evap}$	3.22 MW	$\sum \dot{Q}_{cond}$[a]	2.62 MW
χ	71%	$X/Y/Z_{evap}$	0.78/1.82/0.17 m	$X/Y/Z_{cond}$	1.56/0.46/0.12 m
$\dot{W}_{net,orc}$	571 kW	m_{evap}	132 kg	$\sum m_{cond}$[a]	174 kg
m_{orc}	546 kg	$T_{h,in,evap}$	790 K	$T_{c,in,cond}$	306 K
N_{tg}	49 krpm	$T_{h,out,evap}$	456 K	$T_{c,out,cond}$	345 K
$\dot{m}_{fluid}$	5.40 kg/s	$\Delta p_{h,evap}$	1340 Pa	$\Delta p_{c,cond}$	804 Pa
T_{min}	361 K	$\dot{m}_{h,evap}$	8.81 kg/s	$\sum \dot{m}_{c,cond}$[a]	67.1 kg/s
T_{max}	551 K	$\Delta T_{pp,evap}$	86 K	$\Delta T_{pp,cond}$	29 K
p_{max}	59.5 bar	ϵ_{evap}	80%	ϵ_{cond}	57%
p_{min}	3.1 bar	$\dot{W}_{net,pump}$	69.3 kW		

[a]Summed up over eight condensers.

Downloaded from asmedigitalcollection.asme.org/gasturbinespower/article-pdf/148/11/111002/7625683/gtp-25-1623.pdf by Technische Universiteit Delft - Bibliotheek user on 20 October 2026

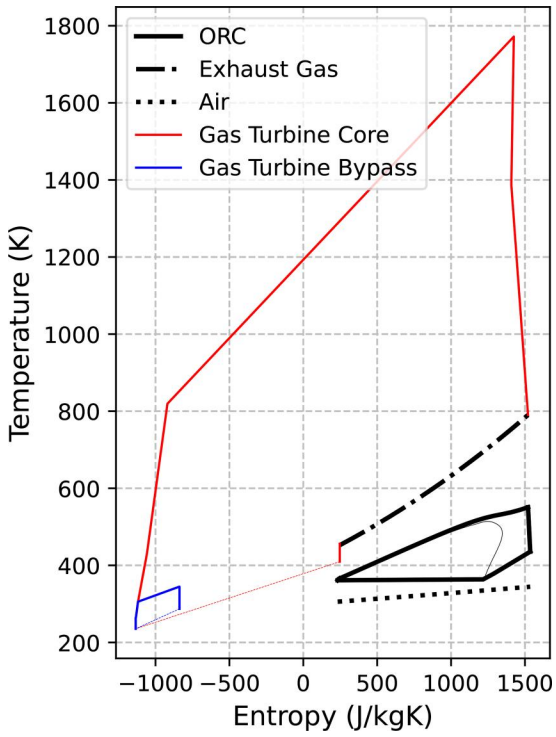


Fig. 9 Temperature–entropy diagram of the CC-TF

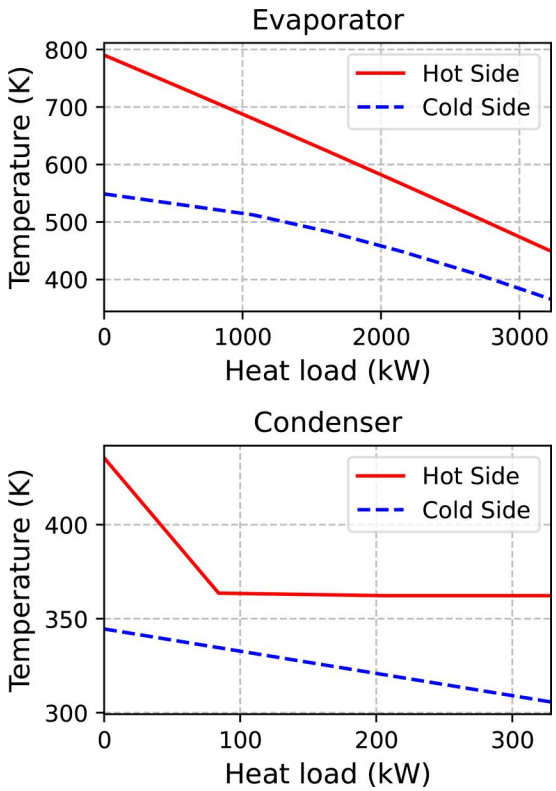


Fig. 10 Temperature–heat load diagram of the evaporator and condenser. The heat load of the condenser is for a single unit.

amount of thermal power from the exhaust of the gas turbine, which often entails a thermal efficiency of the ORC system that is lower than the maximum attainable, as this maximizes the net thermal efficiency of the combined cycle power plant [52, Chap. 3]. This difference is due to all the additional constraints affecting an airborne system and the complex interaction between propulsive system efficiency, weight, and added drag.

The estimated effectiveness (ϵ) of the condenser and evaporator is 57% and 80%, respectively. In the case of the condenser, the moderate effectiveness indicates that the system optimization favors the minimization of the air-side pressure drop over the maximization of the heat transfer area. In addition, the optimized condenser features a high value of mean logarithmic temperature difference. In the case of the evaporator, the relatively high effectiveness indicates that maximization of the system performance favors a maximization of the heat transfer rate over a minimization of the heat exchanger mass. The evaporator recovers 71% of the available exhaust gas thermal power (see Eq. (12)). The relative pressure drops dPqP occurring in the bypass and in the core streams of the gas turbine engine are 2.8% and 5.0%, respectively. The ORC turbine is a high-speed single-stage radial inflow turbine. The rotational speed is 49 krpm, and the Mach number at the outlet of the stator is 1.5. This speed is calculated based on the ORC thermodynamic conditions using the design tool TURBOSIM (see Sec. 2.5). The net power output of the ORC system is 571 kW, which is 27% of the overall engine net power output (see Eq. (3)).

The mass of the WHR ORC unit is 546 kg, which amounts to approximately 30% of the mass of the entire CC-TF engine, which is 1825 kg. The mass-specific power of the ORC unit is 1 kW/kg. As a result of the contribution to shaft power production of the ORC WHR unit, the power capacity of the gas turbine of the CC-TF engine is reduced. The mass flow rate of the CC-TF gas turbine is 36% lower than that of the simple-cycle turbofan engine, and it weighs 25% less.

Compared to the nacelle dimensions of the simple-cycle turbofan engine, the CC-TF engine nacelle features a 15% larger diameter and is 12% shorter. The fan diameter of the CC-TF engine is 18% smaller due to the reduced air mass flow rate. On the one hand, the increase of nacelle diameter is determined according to Eq. (13) as a function of the condenser design variables. On the other hand, the reduction of nacelle length is a result of the reduced engine mass flow rate and, therefore, engine length. Overall, the wetted areas of both the simple-cycle turbofan and the CC-TF engine are very similar, resulting in a similar nacelle drag and values of L/D_{cr}.

The overall thermal efficiency of the CC-TF is higher than that of the simple-cycle turbofan engine. The exchange of 2.62 MW of thermal power from the eight ORC condensers to the bypass air stream increases the bypass duct propulsive efficiency by 13% and the specific thrust of the engine at cruise ST_{cr} by 30%.

Despite this increase in propulsive efficiency, the thrust contribution of the CC-TF engine during cruise is 58% and therefore smaller than for the simple-cycle turbofan engine. This can be attributed to the addition of the WHR system, resulting in a lower mass flow rate of the CC-TF engine and, therefore, less thrust generation and a larger mass of the CC-TF engine compared to that of the simple-cycle engine.

In this study, it is assumed that during takeoff the ORC unit is inoperative; thus, there is no heat addition to the bypass stream and consequent increase of specific thrust. To compensate for the reduced engine size, TIT_{rto} is 22% higher than that of the turbofan engine of the reference aircraft and, as a result, the cooling massflow rate of the CC-TF is 167% larger than that of the simple-cycle turbofan engine. This large cooling requirement strongly penalizes CC-TF engine performance during cruise in two ways: (1) by increasing the compression power demand, and (2) by resulting in a higher degradation of the HPT efficiency as estimated using the cooling model of Ref. [30]. As a result, the gas generator efficiency of the CC-TF engine during cruise is 8 absolute percent points lower than that of the simple-cycle turbofan, which is 81%. To limit the penalty that such a large cooling requirement causes to cruise performance, the design variable α_{to} is set to a value of 70%, which is lower than that of the reference turbofan engine. Under these circumstances, contrary to the reference aircraft, the electrical powertrain of the CC-TF aircraft is sized for RTO conditions, and the optimization constraint $g4$ of Eq. (20) is inactive.

Downloaded from asmedigitalcollection.asme.org/gasturbinespower/article-pdf/148/11/111002/7625683/gtp-25-1623.pdf by Technische Universiteit Delft - Bibliotheek user on 20 October 2026

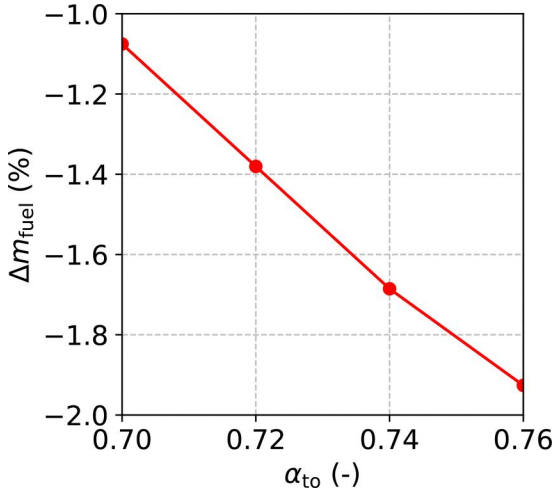


Fig. 11 Relative fuel savings with respect to the optimized CC-TF aircraft obtained with a CC-TF engine adopting a turbine cooling system designed for cruise conditions, as a function of α_{to}

As a result, the electrical powertrain of the CC-TF aircraft is 31% heavier than that of the reference aircraft. This translates into an overall larger aircraft, featuring a 3.8% greater m_{oe} and 1.7% greater m_{mto}. The wing span is therefore slightly larger, and its mass is 2.5% larger. Despite being heavier, the CC-TF aircraft requires less thrust at RTO than the reference aircraft, see Sec. 3.6 for a discussion.

3.3 Sensitivity Study. As explained in Sec. 3.2, the performance of the CC-TF engine during cruise is penalized by the large cooling air demand of the HPT of the gas turbine. The performance of the CC-TF engine might benefit from a cooling system capable of modulating the cooling airflow rate depending on the operating conditions in two ways. First, a large value of the cooling airflow rate is required only at takeoff; therefore, adapting the value to the lower demand due to the lower TIT_{cr} would considerably improve $TSFC_{cr}$. Second, the autonomous modulation of the cooling flow rate depending on the operating condition of the engine (cruise or takeoff) would allow the gas turbine to generate more thrust at takeoff because it would enable the setting of an even higher value of TIT_{rto}. If the CC-TF engine generates more thrust at takeoff, the thrust demand from the electrical powertrain would be lower, resulting in a lighter electrical powertrain. This would contribute to a further reduction in fuel consumption.

A sensitivity study is therefore conducted to provide a preliminary quantification of these benefits. For this purpose, the optimized CC-TF aircraft design (see Sec. 3.2) is reevaluated assuming cruise as the design point of the turbine cooling system and keeping cooling flow rates at takeoff fixed to the values of the optimized design. This simulation is conducted for different values of α_{to}, keeping all other design variables of the CC-TF aircraft at their optimal values. Figure 11 shows the relative fuel-saving potential of the adaptive cooling system with respect to the optimized CC-TF aircraft. The combination of variable cooling air and an increase of α_{to} from a value of 70% to 74% leads to approximately 1.7% fuel savings with respect to the optimized CC-TF aircraft. This translates to 5.4% savings if compared to the fuel consumption of the optimized reference aircraft. The resulting design features a $T_{t,3}$ close to the constrained value of 950 K and a TIT_{rto} of around 2100 K. For values of α_{to} larger than 74%, the $T_{t,3}$ constraint is violated. Furthermore, for values of α_{to} above 76%, no feasible solution is obtained because the value of TIT_{rto} exceeds the upper bound, which is set to 2500 K in PYCYCLE. A more appropriate comparison would be with a simple-cycle turbofan engine also benefiting from variable cooling flow rates; however, due to the lower cooling flow rates, the performance gain would be smaller.

Figure 12 shows the relative change in fuel mass with respect to the optimized CC-TF aircraft as a function of the variation of some important design parameters. These data are calculated based on the optimized CC-TF aircraft design, keeping all design variables fixed and only modifying the parameters of interest one at a time. Figure 12(*a*) shows the effect on fuel consumption of the variation of $dPqP_{byp}$ and $dPqP_{exh}$ relative to their optimized values listed in Table 10. The leftmost points of the chart refer to aircraft designs for which no pressure loss of the heat exchangers is assumed, and only the default values indicated in Table 3 are considered. System performance is more sensitive to pressure loss in the bypass duct than in the exhaust duct, as most of the thrust is generated by the bypass stream. This result highlights the importance of heat exchanger designs optimized for minimum pressure drop. Furthermore, the parametric study shows that, under the assumption of no pressure drop within the channels of heat exchangers (the designs corresponding to the two leftmost points in the curves of Fig. 12(*a*)), fuel savings are around 1%. However, the presented parametric

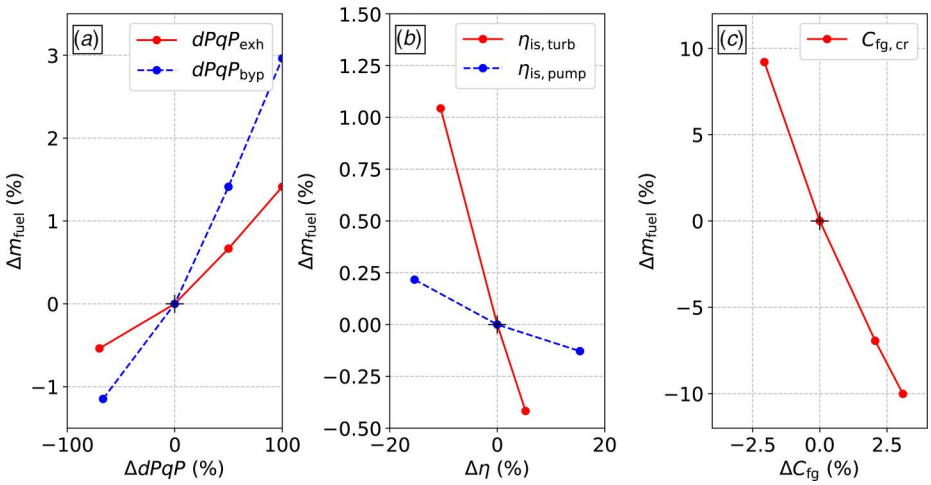


Fig. 12 Results of a sensitivity study showing the relative change of fuel mass (Δm_{fuel}) as a function of selected parameters with respect to the optimized CC-TF aircraft. (*a*) Δm_{fuel} as a function of the relative pressure drop in the exhaust and bypass duct. (*b*) Δm_{fuel} as a function of the relative change in ORC turbomachinery isentropic efficiency. (*c*) Δm_{fuel} as a function of the relative change in gas turbine and nozzle gross thrust coefficient during cruise.

Downloaded from asmedigitalcollection.asme.org/gasturbinespower/article-pdf/148/11/111002/7625683/gtp-25-1623.pdf by Technische Universiteit Delft - Bibliotheek user on 20 October 2026

Table 13 Relevant aircraft parameters resulting from the simulation of three fully turboelectric aircraft for different values of the gross thrust coefficient

Parameter	FT-1	FT-2	FT-3
$C_{fg,cr}$	100%	99.7%	97%
$\eta_{prop,df,cr}$	79.7%	78.5%	67.9%
m_{mto} (t)	70.1	70.5	74.2
m_{oe} (t)	42.8	42.9	44.0
m_{pt} (t)	9.21	9.27	9.96
m_{fuel} (t)	13.7	14.0	16.6

study only considers the effect of dPqP on gas turbine performance. A larger reduction of fuel consumption might be achieved if the CC-TF engine is optimized by considering more advanced heat exchanger technology, allowing for even lower gas-side pressure drops. In this case, the CC-TF engine could be equipped with larger heat exchangers, which would enable higher heat transfer rates, higher ORC system efficiency, and more heat addition to the bypass duct.

Figure 12(*b*) displays the effect on fuel consumption of the variation of ORC turbomachinery efficiency relative to their reference values given in Table 2. The rightmost point of the $\eta_{is,turb}$ curve refers to the fuel consumption in case the isentropic efficiency of the turbine is 100%. System performance is more sensitive to a variation of turbine efficiency than to that of the pump. This result indicates that to maximize system efficiency, it is important that turbomachines are optimized.

Figure 12(*c*) reports the effect on fuel consumption of a variation of the nozzle gross thrust coefficient during cruise ($C_{fg,cr}$) with respect to the reference values given in Table 3 and in Sec. 2.7.1. The rightmost point of the curve refers to a design for which $C_{fg,cr} = 100\%$. Since the sensitivity of fuel consumption to this parameter is very high, an additional analysis is performed, and a discussion on how this parameter affects aircraft performance, and possibly the feasibility of turboelectric aircraft, follows.

Table 13 lists simulation results obtained with the ARENA framework for three different fully turboelectric (FT-1, FT-2, and FT-3) aircraft employing different values of $C_{fg,cr}$. The powertrain architecture of these aircraft is similar to the one described in Sec. 2.3, with the exception that it is powered by simple-cycle turboshaft engines, and besides a small amount of turboshaft residual thrust, the entire thrust is generated by the distributed propulsion system. The calculations are based on the same technology assumptions and most of the modeling assumptions used to model the partial-turboelectric aircraft concept described in this work. The only difference is that the aircraft performance is simulated only during cruise and the electrical powertrain mass and the engine mass are determined based on the methodology presented in Ref. [12]. The turboshaft engines adopt the same thermodynamic cycle specifications, i.e., $OPR_{cr} = 45$ and $TIT_{cr} = 1600\,K$. This combination of OPR_{cr} and TIT_{cr} results in maximized engine efficiency at cruise while fulfilling the constraint that $T_{t3,rto} \leq 950\,K$.

The results of aircraft FT-1 presented in Table 13 are based on $C_{fg,cr} = 100\%$, yielding $m_{fuel} = 13.7\,t$. Aircraft FT-2 adopts the value $C_{fg,cr} = 99.7\%$, which is the value used in the work documented in Ref. [35] for the simulation of the NASA N+3 geared turbofan engine, and by Refs. [53] and [54] for the analysis of two fully turboelectric aircraft concepts. Compared with the FT-1 aircraft, a $C_{fg,cr}$ reduction by 0.3% increases m_{fuel} by 2.2%. The FT-3 aircraft is characterized by $C_{fg,cr} = 97\%$, which is the same value used in this study (see Sec. 2.7.1). Compared with the FT-1 aircraft, a reduction of $C_{fg,cr}$ of 3% increases m_{fuel} by 21.2%.

The comparison of the performance calculated for these three fully turboelectric configurations with the performance estimated for the optimized partial-turboelectric reference aircraft presented in Sec. 3.1 shows that the partial-turboelectric aircraft achieves a 22.2% fuel reduction with respect to the fuel consumption calculated for the FT-3 aircraft, and its fuel consumption is even lower than that of the FT-1 aircraft. The better performance of the partial-turboelectric aircraft is mainly due to the lower mass of the electrical powertrain. Based on this analysis, the following two conclusions can be drawn. First, the feasibility of turboelectric aircraft concepts strongly depends on the value of C_{fg}. Second, there seems to be no consensus in the literature on appropriate values for C_{fg}. Notably, (i) Refs. [35], [53], and [54] do not justify the assumption of the high value taken for C_{fg}, namely, 99.7%, (ii) Ref. [15] does not provide any information on the selected value C_{fg}, and (iii) Ref. [31, Part C, Chap. 1] reports a mean value of C_{fg} of 94% without information regarding its dependency on the operating point. In this respect, the most comprehensive information in the form of experimental data on the variation of nozzle performance with pressure ratio and altitude is reported in Refs. [21] and [55].

3.4 Comparison of the Combined-Cycle Turbofan and Combined-Cycle Turboshaft Engine Concepts. As mentioned in Sec. 1, the CC-TS engine concept integrates a turboshaft engine and an ORC waste heat recovery unit. Its fuel efficiency was previously investigated for a fully turboelectric aircraft designed for the same TLARs and distributed propulsion configuration considered in this work [12]. As in the CC-TF aircraft, the CC-TS engines are housed in pods mounted to the tail cone of the fuselage via pylons. However, although both concepts employ the same heat exchanger topologies for the ORC unit, they differ in their prime mover configuration and in the architecture adopted for system integration within the engine nacelle.

The CC-TS engine features two condensers integrated into separate ram-air ducts located at the top and bottom of the engine nacelle. The evaporator of the CC-TS engine features a square frontal area and is located in the exhaust duct of the turboshaft engine, and it is arranged perpendicular to the exhaust gases. Based on this architecture, the CC-TS engine achieves a reduction in fuel consumption of 1.5% with respect to a fully turboelectric aircraft adopting simple-cycle turboshaft engines. Instead, the CC-TF engine integrated into the powertrain of a partial-turboelectric aircraft achieves a fuel savings reduction of 4%. The combined frontal area of the optimized condenser layout of the CC-TF aircraft is 90% larger than the frontal area of the two condensers of the CC-TS engine, and the combined air mass flow rate is 280% larger. Since the mass flow rate increases more than the frontal area, the condensers of the CC-TF engine are subjected to higher air velocity, resulting in an increase in air-side relative pressure drop by approximately 0.5 absolute percent points. At the same time, the larger heat capacity rate of the cold side of the condenser allows for a reduction of $T_{min,orc}$ and $\Delta T_{pp,cond}$. This improves the $\eta_{net,orc}$ of the ORC system equipping the CC-TF engine by 0.5 absolute percent points if compared to the ORC unit of the CC-TS engine [12]. Furthermore, the larger condenser heat transfer area and air mass flow rate, combined with the lower temperatures, increase the heat transfer rate by 60%.

The mass flow rate of the exhaust gas of the CC-TF engine is 25% lower than that of the CC-TS engine, and the exhaust gas temperature of 790 K is 123 K higher than that of the CC-TS engine. The exhaust gas temperature of the CC-TF engine is higher than that of the CC-TS engine because its TIT_{cr} is 170 K higher. However, the amount of available thermal power at the outlet of the last turbine stage of both engines is similar. The lower exhaust gas mass flow rate, in combination with a 17% larger evaporator frontal area, results in a $dPqP_{exh}$ which is lower by approximately one absolute percent point if compared to the value calculated for the CC-TS engine. Furthermore, the larger heat transfer area and the larger temperature difference between the exhaust gas entering the evaporator and the ORC working fluid result in a heat transfer rate that is 66% greater if compared to that computed for the CC-TS engine. As a result of these effects, the value of $\dot{W}_{net,orc}$ estimated for the CC-TF engine is 70% larger than that computed for the CC-TS engine. Furthermore, the contribution provided by the WHR system to the total electrical power demand of a single engine during cruise

Downloaded from asmedigitalcollection.asme.org/gasturbinespower/article-pdf/148/11/111002/7625683/gtp-25-1623.pdf by Technische Universiteit Delft - Bibliotheek user on 20 October 2026

is 27% for the CC-TF engine, a value much larger than the 6.6% estimated for the CC-TS engine.

Finally, note that the larger space for the ORC condenser in the CC-TF engine configuration does not fully account for its better performance. If a ring-shaped ram-air duct is integrated into the engine nacelle of the CC-TS engine, so that this configuration benefits from an increased condenser area as in the CC-TF engine, and the design is re-optimized based on the same methods and modeling assumptions as in Ref. [12]—except for nacelle sizing, which follows the method described in Sec. 2.6—the resulting fuel savings of the CC-TS-based configuration relative to the reference aircraft amount to 2.3%.

3.5 Comparison of the Combined-Cycle Turbofan Engine With the NASA N+3 Turbofan Engine. As discussed in Sec. 3.2, the propulsive efficiency of CC-TF engines greatly benefits from the heat addition in the bypass duct. The bypass propulsive efficiency as defined by Eq. (7) attains similar values as the N+3 turbofan engine concept [35], which features a bypass ratio of around 24 during cruise. However, the specific thrust of the CC-TF engine is double that of the N+3 engine, resulting in a more compact engine. Furthermore, the partial-turboelectric propulsion system relying on the CC-TF engine achieves a $TSFC_{cr}$ of 13.5 mg/N·s, which is close to the value of 13.1 mg/N·s reported for the N+3 turbofan engine. This result highlights that the partial-turboelectric powertrain, whose prime movers are CC-TF engines, can compete with conventional propulsion system architectures. This consideration is strengthened by the fact that the study detailed in Ref. [35] is based on assumptions associated with more advanced technology, e.g., the use of $C_{fg,cr} = 99.7\%$ instead of $C_{fg,cr} = 97\%$, $\eta_{poly,fan} = 97\%$ instead of $\eta_{poly,fan} = 95\%$, as well as assuming ceramic matrix composite materials for both HPT stator and rotor blades, as opposed to using it for the stator only, as it is assumed in the study regarding the CC-TF engine documented here.

3.6 Additional Considerations on Environmental Impact and on Methodology Limitations. The objective of this work is to identify a propulsion system for passenger aircraft that reduces mission fuel consumption and therefore the emission of the long-lived greenhouse gas CO_2. However, there is a clear consensus in research that a significant share of the contribution of aviation to global warming is associated with non-CO_2 effects caused by the emissions of NO_x and water vapor at high altitude [56]. A suitable metric for the environmental impact of aviation can be the average temperature response over a timeframe of 100 years (ATR_{100}) [57]. The authors of Ref. [58] obtained an aircraft preliminary design for minimized ATR_{100}, which (i) flies at a lower altitude and slower speed if compared to aircraft optimized for minimum operating costs that are the standard nowadays, and (ii) features gas turbine engines with lower OPR and TIT to reduce NO_x emissions. Therefore, the fuel consumption of such aircraft is larger than that of an aircraft optimized for minimum fuel consumption. The adoption of a WHR system for this type of engine, conceived to minimize NO_x emissions, could reduce the penalty of higher fuel consumption.

The design of aircraft for minimum environmental impact requires a multidisciplinary analysis that considers the airframe design, mission profile, and propulsion system design as fully interconnected systems. However, currently, the capabilities of the ARENA framework concerning aircraft design are limited. The available aircraft design method relies on previously computed values of airframe masses and aerodynamic coefficients and only considers the resizing of the wing and the variation of engine nacelle drag. Aircraft constraints analysis is not performed, and fixed values for wing-loading and power-loading need to be provided. The impact of the propulsion system on aircraft size and aerodynamics is only partially considered. For example, the variation in size, the redistribution, and/or the change in the number of the ducted fans affect aerodynamic performance. Similarly, a variation of the position of the center-of-gravity and the resulting requirements on empennage sizing are not considered. These limitations affect the analysis documented here. Therefore, the conclusions drawn from the results of this work are limited to the design of the propulsion system and should not be taken as an integral assessment of the potential of the aircraft concept.

The limited aircraft design capabilities of the ARENA framework also affect the estimation of the value of takeoff thrust ($F_{net,rto}$). The value of $F_{net,rto}$ is obtained using Eq. (1). This equation implies that more takeoff thrust is required for a given value of power-loading and aircraft mass if the propulsive efficiency is higher. For this reason, despite the CC-TF aircraft being heavier and having a lower value of $\eta_{prop,df,rto}$ than the reference aircraft, its $F_{net,rto}$ is smaller. This result is counterintuitive. The correct approach is to perform a constraints analysis to obtain the value of $F_{net,rto}$. Subsequently, the required shaft power can be determined based on this value and the value of $\eta_{prop,df,rto}$.

4 Conclusions

The research documented here concerns the fuel-saving potential of replacing the simple-cycle turbofan engines of a partial-turboelectric aircraft with CC-TF engines. The CC-TF employs a waste heat recovery system based on a newly conceived aerospace-grade ORC unit, which converts the thermal energy of the engine exhaust into additional electrical power via a turbogenerator. The bottoming cycle features a single evaporator placed in the exhaust duct of the gas turbine core and eight condensers arranged in the gas turbine bypass duct downstream of the fan. The effect of adopting this novel propulsion system concept on the fuel consumption of a partial-turboelectric aircraft is analyzed using a multidisciplinary simulation software suite named ARENA framework. These preliminary results indicate that fuel savings of approximately 4% are possible if CC-TF engines are the primary movers instead of simple-cycle turbofan engines. Based on the information presented in this study, the following conclusions can be drawn:

(1) The addition of 2.6 MW of thermal energy to the bypass stream of the CC-TF engine increases its specific thrust by 30% and the bypass propulsive efficiency by 13% at cruise if compared to a simple-cycle turbofan engine. The bypass propulsive efficiency is defined by the thrust power generated by the bypass stream divided by the power required to compress the bypass air. A comparison with the CC-TS engine concept utilizing condensers placed in ram-air ducts shows that the integration of the condensers in the bypass duct of a turbofan engine is considerably more effective due to the air compression.

(2) The ORC waste heat recovery system allows for a lower power capacity of the gas turbine engine at cruise because of the additional power generated by the ORC unit. However, the performance of the CC-TF is negatively affected during off-design operations because the WHR system may contribute less power. For example, to generate the required thrust at takeoff, the turbine inlet temperature of the CC-TF needs to be 20% higher than that of a simple-cycle turbofan engine because the ORC unit does not contribute any power. This increases turbine cooling air demand and reduces the achievable performance during cruise.

(3) The lift-to-drag ratio of the aircraft is unaffected by the adoption of the CC-TF engine configuration. The lower length of the smaller power capacity gas turbine engine, in combination with the larger nacelle diameter due to the addition of the condensers, results in a wet area and drag that are similar to those of the simple-cycle turbofan engine.

(4) The mission fuel consumption varies by approximately 4% for an absolute change in nozzle gross thrust coefficient of 1%. Given the large sensitivity, it is therefore important that reliable values of the gross thrust coefficient of the nozzle of turbofan engines and ducted fans are selected.

Downloaded from asmedigitalcollection.asme.org/gasturbinespower/article-pdf/148/11/111002/7625683/gtp-25-1623.pdf by Technische Universiteit Delft - Bibliotheek user on 20 October 2026

The work summarized in this chapter enlarges the rather limited knowledge base regarding the design of airborne ORC systems and their potential effect on future engine and aircraft concepts. Based on these findings, it is suggested that further research will aim at:

(1) investigating the effect of different ORC working fluids on system performance and other operational and safety aspects,
(2) estimating the potential benefit of mechanically coupling the ORC turbine with the low-speed shaft of the gas turbine engine,
(3) studying more advanced heat exchanger topologies and optimized channel shapes and their integration with the prime mover,
(4) assessing the aerodynamic penalty associated with the installation of the heat exchangers in the engine core and cooling air ducts with CFD simulations,
(5) expanding the capability of the ARENA framework regarding the aircraft design features to better evaluate and optimize the effect of the propulsion system on aircraft performance,
(6) developing a dynamic model for the ORC system to estimate the phase of the aircraft mission from which fuel savings are enabled by the WHR unit, as well as its potential contribution to aircraft propulsion during descent, and
(7) analyzing the potential of ORC systems as a means to increase the performance of aircraft optimized for minimum environmental impact.

Conflict of Interest

There are no conflicts of interest.

Funding Data

Applied and Engineering Sciences Division (TTW) of the Dutch Organization for Scientific Research (NWO), Open Technology Program of the Ministry of Economic Affairs (Grant No. 17906; Funder ID: 10.13039/501100003246).

Data Availability Statement

The datasets generated and supporting the findings of this article are obtainable from the corresponding author upon reasonable request.

Appendix A: Reference Engine Thermodynamic Cycle Data

PERFORMANCE SUMMARY

Operating Point	MN (-)	alt (km)	dTisa (K)	W0 (kg/s)	Fn (kN)	Fg (kN)	FAR (-)	TIT (K)	BPR (-)	OPR (-)	Pwr (kW)	eta_gg (-)
DESIGN	0.780	10.457	15.000	116.368	13.105	41.019	0.018	1470.252	7.500	50.828	1319.136	0.810

FLOW STATIONS

Flow Station	Pt (Pa)	Tt (K)	ht (kJ/kg)	S (kJ/(kg*K))	P_s (Pa)	W (kg/s)	MN (-)	V (m/s)	area (m**2)
ambient	36651.510	263.858	-38.761	7.032	24637.122	1.000	0.780	239.878	0.011
inlet exit	36578.207	263.858	-38.761	7.033	28713.783	116.368	0.600	188.750	1.512
fan exit	57094.754	301.022	-1.444	7.038	48000.646	116.368	0.500	169.723	1.171
splitter bypass exit	57094.754	301.022	-1.444	7.038	51067.542	13.690	0.400	136.952	0.163
splitter core exit	57094.754	301.022	-1.444	7.038	48000.646	102.677	0.500	169.723	1.034
LPC exit	171284.261	422.006	120.727	7.064	153767.583	13.690	0.400	161.874	0.065
HPC exit	1859194.874	860.077	585.890	7.132	1668112.276	13.301	0.400	227.763	0.008
burner exit	1784827.079	1470.252	544.734	7.869	1737355.383	13.540	0.200	147.372	0.022
HPT exit	413077.406	1080.138	86.870	7.908	372019.776	13.929	0.400	252.627	0.045
LPT exit	39804.132	618.488	-438.638	7.948	35659.051	13.929	0.400	194.019	0.347
exhaust duct exit	39207.070	618.488	-438.638	7.953	36810.955	13.929	0.300	146.377	0.451
core nozzle exit	39089.448	618.488	-438.638	7.953	24637.122	13.929	0.847	392.797	0.226
bypass duct exit	56523.806	301.022	-1.444	7.040	53131.199	102.677	0.300	103.415	1.581
bypass nozzle exit	56354.235	301.022	-1.444	7.041	29692.647	102.677	1.000	317.561	0.781

TURBOMACHINERY PROPERTIES

Component	Wred (kg/s)	Pr (-)	eta_a (-)	eta_p (-)	pwr (kW)	Nmech (rpm)	Nc (rpm)	SMN (-)	SMW (-)
FAN	308.463	1.561	0.959	0.961	-4342.463	4117.806	4303.189	29.211	23.194
LPC	24.833	3.000	0.908	0.923	-1672.570	15000.000	14675.783	12.234	11.941
HPC	9.801	10.854	0.878	0.910	-6368.254	26000.000	21484.408	22.598	22.468
HPT	2.691	4.321	0.902	0.885	6393.830	26000.000	505.407	N/A	N/A
LPT	10.252	10.378	0.956	0.941	7320.024	15000.000	340.185	N/A	N/A

SECONDARY FLOWS

Bleed	Wb/Win (-)	W (kg/s)	Tt (K)	Pt (Pa)
LPC blowoff	0.000	0.000	1.000	57094.754
HPT chargeable	0.000	1.000	1.000	1859194.874
HPT non-chargeable	0.028	1.000	1.000	1859194.874

NOZZLE PROPERTIES

Nozzle	PR (-)	Ath (m**2)	MNth (-)	V (m/s)	Fg (kN)	Cfg (-)
core_nozz	1.587	0.226	0.847	392.797	5.323	0.970
byp_nozz	2.287	0.781	1.000	317.561	35.696	0.970

Fig. 13 Thermodynamic cycle data of the reference turbofan engine at the cruise operating point (thermodynamic design point)

Downloaded from asmedigitalcollection.asme.org/gasturbinespower/article-pdf/148/11/111002/7625683/gtp-25-1623.pdf by Technische Universiteit Delft - Bibliotheek user on 20 October 2026

PERFORMANCE SUMMARY

Operating Point	MN (-)	alt (km)	dTisa (K)	W0 (kg/s)	Fn (kN)	Fg (kN)	FAR (-)	TIT (K)	BPR (-)	OPR (-)	Pwr (kW)	eta_gg (-)
RTO	0.250	0.000	15.000	288.666	55.372	80.559	0.019	1571.947	7.991	40.594	1344.705	0.716

FLOW STATIONS

Flow Station	Pt (Pa)	Tt (K)	ht (kJ/kg)S	(kJ/(kg*K))	P_s (Pa)	W (kg/s)	MN (-)	V (m/s)	area (m**2)
ambient	106129.121	306.939	4.499	6.880	101324.664	1.000	0.250	87.253	0.010
inlet exit	105916.863	306.939	4.499	6.881	86510.083	288.666	0.537	183.258	1.512
fan exit	156501.146	344.485	42.288	6.885	133546.796	288.666	0.479	174.074	1.171
splitter bypass exit	156501.146	344.485	42.288	6.885	143195.374	32.107	0.360	132.157	0.163
splitter core exit	156501.146	344.485	42.288	6.885	133155.423	256.559	0.483	175.700	1.034
LPC exit	404223.297	460.559	160.029	6.907	363983.815	30.576	0.395	166.769	0.065
HPC exit	4299614.585	926.216	659.947	6.974	3864459.792	29.706	0.401	236.554	0.008
burner exit	4127630.001	1571.947	614.090	7.719	4127575.689	30.283	0.004	3.310	1.000
HPT exit	955067.384	1159.847	122.749	7.758	861868.019	31.153	0.401	262.008	0.045
LPT exit	121591.171	718.162	-390.467	7.795	114208.120	31.153	0.304	159.341	0.347
exhaust duct exit	121591.171	718.162	-390.467	7.795	117197.863	31.153	0.229	120.255	0.451
core nozzle exit	121226.397	718.162	-390.467	7.796	101324.664	31.153	0.519	267.963	0.226
bypass duct exit	156501.146	344.485	42.288	6.885	148079.577	256.559	0.289	106.513	1.581
bypass nozzle exit	156031.643	344.485	42.288	6.885	101324.664	256.559	0.810	283.446	0.781

TURBOMACHINERY PROPERTIES

Component	Wred (kg/s)	Pr (-)	eta_a (-)	eta_p (-)	pwr (kW)	Nmech (rpm)	Nc (rpm)	SMN (-)	SMW (-)
FAN	285.012	1.478	0.967	0.970	-10908.335	4097.333	3969.949	32.495	24.052
LPC	22.729	2.583	0.913	0.925	-3780.346	14925.420	13650.577	15.535	15.000
HPC	9.690	10.637	0.879	0.909	-15285.318	27080.390	21420.103	23.589	23.563
HPT	2.691	4.322	0.902	0.886	15346.705	27080.390	509.096	N/A	N/A
LPT	10.276	7.855	0.952	0.938	15988.257	14925.420	326.656	N/A	N/A

SECONDARY FLOWS

Bleed	Wb/Win (-)	W (kg/s)	Tt (K)	Pt (Pa)
LPC blowoff	0.048	0.000	1.000	156501.146
HPT chargeable	0.000	1.000	1.000	4299614.585
HPT non-chargeable	0.028	1.000	1.000	4299614.585

NOZZLE PROPERTIES

Nozzle	PR (-)	Ath (m**2)	MNth (-)	V (m/s)	Fg (kN)	Cfg (-)
core_nozz	1.196	0.226	0.519	267.963	8.330	0.990
byp_nozz	1.540	0.781	0.810	283.446	72.229	0.990

Fig. 14 Thermodynamic cycle data of the reference turbofan engine at the RTO operating point

PERFORMANCE SUMMARY

Operating Point	MN (-)	alt (km)	dTisa (K)	W0 (kg/s)	Fn (kN)	Fg (kN)	FAR (-)	TIT (K)	BPR (-)	OPR (-)	Pwr (kW)	eta_gg (-)
SLS	0.000	0.000	15.000	267.672	69.215	69.216	0.019	1533.363	7.904	38.913	894.022	0.704

FLOW STATIONS

Flow Station	Pt (Pa)	Tt (K)	ht (kJ/kg)S	(kJ/(kg*K))	P_s (Pa)	W (kg/s)	MN (-)	V (m/s)	area (m**2)
ambient	101324.664	303.150	0.693	6.880	101324.664	1.000	0.000	0.003	245.801
inlet exit	101122.014	303.150	0.693	6.881	84601.232	267.672	0.507	172.620	1.512
fan exit	148099.607	339.478	37.240	6.886	127366.581	267.672	0.462	167.214	1.171
splitter bypass exit	148099.607	339.478	37.240	6.886	135121.725	30.062	0.354	129.205	0.163
splitter core exit	148099.607	339.478	37.240	6.886	127067.529	237.609	0.466	168.508	1.034
LPC exit	373618.546	451.035	150.291	6.908	335735.662	28.352	0.392	164.163	0.065
HPC exit	3934967.476	905.975	637.204	6.975	3527387.049	27.545	0.403	234.989	0.008
burner exit	3777568.777	1533.363	593.387	7.710	3777522.054	28.061	0.004	3.269	1.000
HPT exit	873125.954	1129.373	114.484	7.750	785134.395	28.868	0.402	259.405	0.045
LPT exit	118281.868	708.930	-371.644	7.786	112241.881	28.868	0.285	148.586	0.347
exhaust duct exit	118281.868	708.930	-371.644	7.786	114827.624	28.868	0.215	112.367	0.451
core nozzle exit	117927.022	708.930	-371.644	7.787	101324.664	28.868	0.479	246.726	0.226
bypass duct exit	148099.607	339.478	37.240	6.886	139623.434	237.609	0.281	103.060	1.581
bypass nozzle exit	147655.308	339.478	37.240	6.887	101324.664	237.609	0.751	263.022	0.781

TURBOMACHINERY PROPERTIES

Component	Wred (kg/s)	Pr (-)	eta_a (-)	eta_p (-)	pwr (kW)	Nmech (rpm)	Nc (rpm)	SMN (-)	SMW (-)
FAN	275.101	1.465	0.953	0.954	-9782.677	4012.761	3912.225	30.438	21.911
LPC	22.324	2.523	0.913	0.925	-3398.558	14617.348	13467.029	15.612	15.000
HPC	9.620	10.532	0.879	0.910	-13804.911	26749.279	21380.427	23.825	23.904
HPT	2.691	4.326	0.902	0.886	13860.352	26749.279	509.159	N/A	N/A
LPT	10.278	7.382	0.950	0.937	14033.565	14617.348	324.201	N/A	N/A

SECONDARY FLOWS

Bleed	Wb/Win (-)	W (kg/s)	Tt (K)	Pt (Pa)
LPC blowoff	0.057	0.000	1.000	148099.607
HPT chargeable	0.000	1.000	1.000	3934967.476
HPT non-chargeable	0.028	1.000	1.000	3934967.476

NOZZLE PROPERTIES

Nozzle	PR (-)	Ath (m**2)	MNth (-)	V (m/s)	Fg (kN)	Cfg (-)
core_nozz	1.164	0.226	0.479	246.726	7.122	0.990
byp_nozz	1.457	0.781	0.751	263.022	62.094	0.990

Fig. 15 Thermodynamic cycle data of the reference turbofan engine at the SLS operating point

Downloaded from asmedigitalcollection.asme.org/gasturbinespower/article-pdf/148/11/111002/7625683/gtp-25-1623.pdf by Technische Universiteit Delft - Bibliotheek user on 20 October 2026

Appendix B: Combined-Cycle Turbofan Engine Thermodynamic Cycle Data

PERFORMANCE SUMMARY

Operating Point	MN (-)	alt (km)	dTisa (K)	W0 (kg/s)	Fn (kN)	Fg (kN)	FAR (-)	TIT (K)	BPR (-)	OPR (-)	Pwr (kW)	eta_gg (-)
DESIGN	0.780	10.418	15.000	75.768	9.833	28.018	0.029	1771.867	7.820	42.187	2135.579	0.734

FLOW STATIONS

Flow Station	Pt (Pa)	Tt (K)	ht (kJ/kg)	S (kJ/(kg*K))	P_s (Pa)	W (kg/s)	MN (-)	V (m/s)	area (m**2)
ambient	36880.010	264.142	-38.475	7.031	24786.789	1.000	0.780	240.008	0.011
inlet exit	36806.250	264.142	-38.475	7.032	28875.795	75.768	0.600	188.851	0.979
fan exit	60358.938	305.698	3.252	7.039	50553.659	75.768	0.500	171.030	0.730
splitter bypass exit	60358.938	305.698	3.252	7.039	53791.052	8.591	0.400	138.007	0.098
splitter core exit	60358.938	305.698	3.252	7.039	50553.659	67.177	0.500	171.030	0.647
LPC exit	181076.813	429.766	128.619	7.066	162370.460	8.591	0.400	163.323	0.039
HPC exit	1552735.075	819.382	540.793	7.130	1394380.740	7.836	0.400	222.600	0.006
burner exit	1490625.672	1771.867	475.564	8.208	1452249.627	8.066	0.200	160.436	0.018
HPT exit	489601.964	1387.723	78.115	8.200	441259.950	8.821	0.400	283.891	0.027
LPT exit	38629.842	790.223	-643.802	8.252	34720.676	8.821	0.400	217.489	0.258
exhaust duct exit	36713.752	456.037	-1009.807	7.665	34620.894	8.821	0.300	126.221	0.260
core nozzle exit	36603.611	456.037	-1009.807	7.666	24786.789	8.821	0.777	312.770	0.134
bypass duct exit	58649.868	344.567	42.372	7.167	55121.125	67.177	0.300	110.591	1.070
bypass nozzle exit	58473.918	344.567	42.372	7.168	30731.266	67.177	1.000	339.743	0.529

TURBOMACHINERY PROPERTIES

Component	Wred (kg/s)	Pr (-)	eta_a (-)	eta_p (-)	pwr (kW)	Nmech (rpm)	Nc (rpm)	SMN (-)	SMW (-)
FAN	199.707	1.640	0.954	0.955	-3161.615	5119.082	5346.657	29.211	23.194
LPC	14.854	3.000	0.906	0.920	-1077.010	15000.000	14563.107	12.234	11.941
HPC	5.871	8.575	0.877	0.906	-3540.930	25000.000	20470.734	22.598	22.468
HPT	2.107	3.045	0.867	0.851	3555.150	25000.000	442.678	N/A	N/A
LPT	6.208	12.674	0.947	0.929	6368.061	15000.000	300.126	N/A	N/A

SECONDARY FLOWS

Bleed	Wb/Win (-)	W (kg/s)	Tt (K)	Pt (Pa)
LPC blowoff	0.000	0.000	1.000	60358.938
HPT chargeable	0.021	1.000	1.000	1552735.075
HPT non-chargeable	0.066	1.000	1.000	1552735.075

NOZZLE PROPERTIES

Nozzle	PR (-)	Ath (m**2)	MNth (-)	V (m/s)	Fg (kN)	Cfg (-)
core_nozz	1.477	0.134	0.777	312.770	2.686	0.970
byp_nozz	2.359	0.529	1.000	339.743	25.332	0.970

Fig. 16 Thermodynamic cycle data of the CC-TF engine at the cruise operating point (thermodynamic design point)

PERFORMANCE SUMMARY

eta_th	W_turb [kW]	W_pump [kW]	m [kg/s]	W_in [kW]
0.186	670.0	69.4	5.41	32287

FLOW STATIONS

cyclopentane	P [bar]	T [C]	h [kJ/kg]	s [kJ/kg.K]
HRSG out	58.9	277.7	689.57	1.521
Turb out	3.37	162.4	565.74	1.536
Condenser out	3.12	88.2	79.82	0.233
Pump out	9.54	92.6	92.65	0.245

Exhaust	P [bar]	T [C]	h [kJ/kg]	s [kJ/kg.K]
HRSG in:	0.3861	516.8	-960.65	8.082
HRSG out:	0.3727	178.8	-1326.39	7.490

Ram air	P [bar]	T [C]	h [kJ/kg]	s [kJ/kg.K]
Cond in:	0.6039	32.6	432.155	4.055
Cond out:	0.5959	71.4	471.267	4.179

Fig. 17 ORC unit state point data at the cruise operating point (thermodynamic design point)

Downloaded from asmedigitalcollection.asme.org/gasturbinespower/article-pdf/148/11/111002/7625683/gtp-25-1623.pdf by Technische Universiteit Delft - Bibliotheek user on 20 October 2026

PERFORMANCE SUMMARY

Operating Point	MN (-)	alt (km)	dTisa (K)	W0 (kg/s)	Fn (kN)	Fg (kN)	FAR (-)	TIT (K)	BPR (-)	OPR (-)	Pwr (kW)	eta_gg (-)
RTO	0.250	0.000	15.000	205.004	45.554	63.441	0.034	1964.760	8.249	37.860	3357.468	0.665

FLOW STATIONS

Flow Station	Pt (Pa)	Tt (K)	ht (kJ/kg)	S (kJ/(kg*K))	P_s (Pa)	W (kg/s)	MN (-)	V (m/s)	area (m**2)
ambient	106129.121	306.939	4.499	6.880	101324.664	1.000	0.250	87.253	0.010
inlet exit	105916.863	306.939	4.499	6.881	81332.130	205.004	0.620	209.900	0.979
fan exit	165325.967	351.702	49.570	6.889	135393.679	205.004	0.541	197.525	0.730
splitter bypass exit	165325.967	351.702	49.570	6.889	148516.987	22.165	0.402	148.762	0.098
splitter core exit	165325.967	351.702	49.570	6.889	134950.823	182.839	0.545	199.147	0.647
LPC exit	484492.572	489.793	189.993	6.918	436966.534	20.982	0.389	169.411	0.039
HPC exit	4010022.469	915.058	647.403	6.981	3603478.595	19.138	0.401	235.160	0.006
burner exit	3849621.570	1964.760	569.469	8.092	3849593.168	19.783	0.003	2.898	1.000
HPT exit	1273353.880	1551.821	130.549	8.082	1153465.522	21.626	0.399	298.050	0.027
LPT exit	141646.230	972.273	-594.495	8.129	134301.594	21.626	0.285	172.047	0.258
exhaust duct exit	139521.537	972.273	-594.495	8.134	132370.438	21.626	0.288	173.299	0.260
core nozzle exit	139102.972	972.273	-594.495	8.134	101324.664	21.626	0.705	412.417	0.134
bypass duct exit	163672.707	351.702	49.570	6.892	154371.822	182.839	0.295	109.706	1.070
bypass nozzle exit	163181.689	351.702	49.570	6.893	101324.664	182.839	0.856	300.611	0.529

TURBOMACHINERY PROPERTIES

Component	Wred (kg/s)	Pr (-)	eta_a (-)	eta_p (-)	pwr (kW)	Nmech (rpm)	Nc (rpm)	SMN (-)	SMW (-)
FAN	202.409	1.561	0.934	0.939	-9239.624	5530.633	5358.688	38.221	31.465
LPC	15.008	2.931	0.900	0.915	-3112.478	16205.931	14668.839	15.314	15.000
HPC	5.721	8.277	0.879	0.907	-9597.254	26512.162	20335.189	23.621	23.803
HPT	2.107	3.023	0.868	0.854	9635.798	26512.162	445.814	N/A	N/A
LPT	6.189	8.990	0.941	0.924	15679.896	16205.931	306.632	N/A	N/A

SECONDARY FLOWS

Bleed	Wb/Win (-)	W (kg/s)	Tt (K)	Pt (Pa)
LPC blowoff	0.053	0.000	1.000	165325.967
HPT chargeable	0.021	1.000	1.000	4010022.469
HPT non-chargeable	0.066	1.000	1.000	4010022.469

NOZZLE PROPERTIES

Nozzle	PR (-)	Ath (m**2)	MNth (-)	V (m/s)	Fg (kN)	Cfg (-)
core_nozz	1.373	0.134	0.705	412.417	8.868	0.990
byp_nozz	1.610	0.529	0.856	300.611	54.573	0.990

Fig. 18 Thermodynamic cycle data of the CC-TF engine at the RTO operating point

PERFORMANCE SUMMARY

Operating Point	MN (-)	alt (km)	dTisa (K)	W0 (kg/s)	Fn (kN)	Fg (kN)	FAR (-)	TIT (K)	BPR (-)	OPR (-)	Pwr (kW)	eta_gg (-)
SLS	0.000	0.000	15.000	194.969	56.943	56.943	0.031	1872.564	8.347	36.259	2225.666	0.667

FLOW STATIONS

Flow Station	Pt (Pa)	Tt (K)	ht (kJ/kg)	S (kJ/(kg*K))	P_s (Pa)	W (kg/s)	MN (-)	V (m/s)	area (m**2)
ambient	101324.664	303.150	0.693	6.880	101324.664	1.000	0.000	0.003	245.801
inlet exit	101122.014	303.150	0.693	6.881	78643.885	194.969	0.607	204.569	0.979
fan exit	158494.136	346.787	44.610	6.887	131158.667	194.969	0.528	191.613	0.730
splitter bypass exit	158494.136	346.787	44.610	6.887	143069.334	20.860	0.390	143.414	0.098
splitter core exit	158494.136	346.787	44.610	6.887	130653.378	174.110	0.533	193.519	0.647
LPC exit	466250.939	482.675	182.671	6.914	423516.250	19.702	0.374	161.969	0.039
HPC exit	3666533.910	889.766	619.005	6.975	3286368.022	17.972	0.407	235.142	0.006
burner exit	3519872.553	1872.564	547.960	8.042	3519847.919	18.528	0.003	2.829	1.000
HPT exit	1162745.019	1473.530	127.984	8.033	1049921.453	20.259	0.399	291.169	0.027
LPT exit	135333.452	928.217	-545.145	8.081	129129.146	20.259	0.271	160.168	0.258
exhaust duct exit	133303.450	928.217	-545.145	8.086	126978.376	20.259	0.274	161.699	0.260
core nozzle exit	132903.540	928.217	-545.145	8.087	101324.664	20.259	0.648	372.776	0.134
bypass duct exit	156909.195	346.787	44.610	6.890	148626.824	174.110	0.290	107.160	1.070
bypass nozzle exit	156438.467	346.787	44.610	6.891	101324.664	174.110	0.815	285.755	0.529

TURBOMACHINERY PROPERTIES

Component	Wred (kg/s)	Pr (-)	eta_a (-)	eta_p (-)	pwr (kW)	Nmech (rpm)	Nc (rpm)	SMN (-)	SMW (-)
FAN	200.381	1.567	0.951	0.955	-8562.615	5387.141	5252.171	37.218	29.867
LPC	14.630	2.942	0.908	0.920	-2879.911	15785.468	14389.168	12.295	12.000
HPC	5.542	7.864	0.880	0.907	-8596.867	26105.878	20170.672	25.765	26.126
HPT	2.107	3.027	0.868	0.854	8631.393	26105.878	449.659	N/A	N/A
LPT	6.187	8.592	0.939	0.922	13637.115	15785.468	306.508	N/A	N/A

SECONDARY FLOWS

Bleed	Wb/Win (-)	W (kg/s)	Tt (K)	Pt (Pa)
LPC blowoff	0.055	0.000	1.000	158494.136
HPT chargeable	0.021	1.000	1.000	3666533.910
HPT non-chargeable	0.066	1.000	1.000	3666533.910

NOZZLE PROPERTIES

Nozzle	PR (-)	Ath (m**2)	MNth (-)	V (m/s)	Fg (kN)	Cfg (-)
core_nozz	1.312	0.134	0.648	372.776	7.519	0.990
byp_nozz	1.544	0.529	0.815	285.755	49.425	0.990

Fig. 19 Thermodynamic cycle data of the CC-TF engine at the SLS operating point

Downloaded from asmedigitalcollection.asme.org/gasturbinespower/article-pdf/148/11/111002/7625683/gtp-25-1623.pdf by Technische Universiteit Delft - Bibliotheek user on 20 October 2026

References

[1] Kyprianidis, K., 2019, "On Gas Turbine Conceptual Design," Ph.D. thesis, Cranfield University, Bedford, UK.
[2] Boggia, S., and Klaus, R., 2005, "Intercooled Recuperated Gas Turbine Engine Concept," AIAA Paper No. 2005-4192.
[3] Xu, L., Kyprianidis, K. G., and Grönstedt, T. U. J., 2013, "Optimization Study of an Intercooled Recuperated Aero-Engine," J. Propul. Power, **29**(2), pp. 424–432.
[4] Pouzolz, R., Schmitz, O., and Klingels, H., 2021, "Evaluation of the Climate Impact Reduction Potential of the Water-Enhanced Turbofan (WET) Concept," Aerospace, **8**(3), p. 59.
[5] Colonna, P., Astolfi, M., van Buijtenen, J., Wieland, C., David, G., Garofalo, F., Baresi, M., Öhman, H., and Klink, W., 2021, "Thermal Energy Harvesting: The Path to Tapping Into a Large CO_2-Free European Power Source," Knowledge Center on Organic Rankine Cycle Technology, Delft, The Netherlands, accessed Aug. 23, 2024, https://kcorc.org/wp-content/uploads/2022/06/Thermal_Energy_-Harvesting_-_the_Path_to_Tapping_into_a_Large_CO2-free_European_Power_Source.pdf
[6] Perullo, C. A., Mavris, D. N., and Fonseca, E., 2013, "An Integrated Assessment of an Organic Rankine Cycle Concept for Use in Onboard Aircraft Power Generation," ASME Paper No. GT2013-95734.
[7] Zarati, K., Maalouf, S., and Isikveren, A. T., 2017, "Potential of the Bottom Organic Rankine Cycle to Recover Energy on Turboprop Engine Architecture," 23rd ISABE Conference, Manchester, UK.
[8] De Servi, C. M., Azzini, L., Pini, M., Gangoli Rao, A., and Colonna, P., 2017, "Exploratory Assessment of a Combined-Cycle Engine Concept for Aircraft Propulsion," First Global Power and Propulsion Forum, https://www.semanticscholar.org/paper/Exploratory-assessment-of-a-combined-cycle-engine-Servi-Azzini/7a752bc4a697fe3366e2e9dc910fb3c39ba18c8d
[9] Jacob, F., Rolt, A. M., Sebastiampillai, J. M., Sethi, V., Belmonte, M., and Cobas, P., 2017, "Performance of a Supercritical CO_2 Bottoming Cycle for Aero Applications," Appl. Sci., **7**(3), p. 255.
[10] Hughes, M., and Olsen, J., 2022, "Fuel Burn Reduction of Hybrid Aircraft Employing an Exhaust Heat Harvesting System," J. Propul. Power, **38**(2), pp. 241–253.
[11] Krempus, D., Beltrame, F., Majer, M., Pini, M., Vos, R., Colonna, P., and De Servi, C. M., 2025, "Organic Rankine Cycle Waste Heat Recovery Systems for Aircraft Auxiliary Power Units," J. Global Power Propul. Soc., **9**, pp. 275–303.
[12] Krempus, D., Beltrame, F., Majer, M., Colonna, P., De Servi, C. M., and Vos, R., 2024, "ORC Waste Heat Recovery System for the Turboshaft Engines of Tuboelectric Aircraft: Correction," Delft University of Technology, Delft, The Netherlands, accessed Aug. 23, 2024, https://research.tudelft.nl/en/publications/orc-waste-heat-recovery-system-for-the-turboshaft-engines-of-turb
[13] Welstead, J., and Felder, J. L., 2016, "Conceptual Design of a Single-Aisle Turboelectric Commercial Transport With Fuselage Boundary Layer Ingestion," AIAA Paper No. 2016-1027.
[14] Chau, T., Kenway, G., and Kiris, C. C., 2022, "Conceptual Exploration of Aircraft Configurations for the SUSAN Electrofan," AIAA Paper No. 2022-2181.
[15] Schmollgruber, P., Donjat, D., Ridel, M., Cafarelli, I., Atinault, O., François, C., and Paluch, B., 2020, "Multidisciplinary Design and Performance of the ONERA Hybrid Electric Distributed Propulsion Concept (Dragon)," AIAA Paper No. 2020-0501.
[16] Gray, J. S., Hwang, J. T., Martins, J. R. R. A., Moore, K. T., and Naylor, B. A., 2019, "OpenMDAO: An Open-Source Framework for Multidisciplinary Design, Analysis, and Optimization," Struct. Multidiscip. Optim., **59**(4), pp. 1075–1104.
[17] Heldenbrand, R. W., and Miller, W. S., 1981, "Regenerative Engine Analysis Program (REAP)," AiResearch Mfg. Co., Phoenix, AZ, Report No. USAAVRADCOM-TR-81-D-2.
[18] Kaiser, S., Schmitz, O., Ziegler, P., and Klingels, H., 2022, "The Water-Enhanced Turbofan as Enabler for Climate-Neutral Aviation," Appl. Sci., **12**(23), p. 12431.
[19] Badger, M., Julien, A., LeBlanc, A. D., Moustapha, S. H., Prabhu, A., and Smailys, A. A., 1993, "The PT6 Engine: 30 Years of Gas Turbine Technology Evolution," ASME Paper No. 93-GT-006.
[20] Torenbeek, E., 2013, *Advanced Aircraft Design*, John Wiley & Sons, Chichester, UK.
[21] Obert, E., 2009, *Aerodynamic Design of Transport Aircraft*, IOS Press, Amsterdam, The Netherlands.
[22] de Vries, R., Brown, M., and Vos, R., 2019, "Preliminary Sizing Method for Hybrid-Electric Distributed-Propulsion Aircraft," J. Aircr., **56**(6), pp. 2172–2188.
[23] Torenbeek, E., 1987, "The Initial Calculation of Range and Mission Fuel During Conceptual Design," Delft University of Technology, Faculty of Aerospace Engineering, Delft, The Netherlands, Report No. LR-525.
[24] Mattingly, J. D., Heiser, W. H., Boyer, K. M., Haven, B. A., and Pratt, D. T., 2018, *Aircraft Engine Design*, 3rd ed., AIAA, Reston, VA.
[25] Golovanov, D., Gerada, D., Sala, G., Degano, M., Trentin, A., Connor, P. H., Xu, Z., et al., 2021, "4-MW Class High-Power-Density Generator for Future Hybrid-Electric Aircraft," IEEE Trans. Transp. Electrif., **7**(4), pp. 2952–2964.
[26] Ridel, M., Nguyen Van, E., Prosvirnova, T., Donjat, D., Seguin, C., and Choy, P., 2021, "DRAGON: Hybrid Electrical Architecture for Distributed Fans Propulsion," MEA Conference, Bordeaux, France, Nov. 9.
[27] Hendricks, E. S., and Gray, J. S., 2019, "pyCycle: A Tool for Efficient Optimization of Gas Turbine Engine Cycles," Aerospace, **6**(8), p. 87.
[28] Samuelsson, S., Gronstedt, T., and Kyprianidis, K. G., 2015, "Consistent Conceptual Design and Performance Modeling of Aero Engines," ASME Paper No. GT2015-43331.
[29] Grieb, H., 2004, *Projektierung von Turboflugtriebwerken*, Birkhäuser Basel, Basel, Switzerland.
[30] Gauntner, J. W., 1980, "Algorithm for Calculating Turbine Cooling Flow and the Resulting Decrease in Turbine Efficiency," NASA Lewis Research Centre, Cleveland, OH, Report No. NASA-TM-81453.
[31] Kurzke, J., and Halliwell, I., 2018, *Propulsion and Power: An Exploration of Gas Turbine Performance Modeling*, Springer International Publishing, Cham, Switzerland.
[32] Greitzer, E. M., Bonnefoy, P., De la Rosa Blanco, E., Dorbian, C., Drela, M., Hall, D., Hansman, R., et al., 2010, "N+3 Aircraft Concept Designs and Trade Studies, Final Report," NASA Glenn Research Center, Cleveland, OH, Report No. NASACR-2010-216794/vol2.
[33] Boersma, I., 2022, "Weight Estimation of Gas Turbine Engines," Master's thesis, Delft University of Technology, Delft, The Netherlands.
[34] Verweij, F., 2023, "Weight Estimation of Turboshaft Engines," Master's thesis, Delft University of Technology, Delft, The Netherlands.
[35] Scott, M. J., Haller, W. J., and Tong, M. T.-H., 2017, "An N+3 Technology Level Reference Propulsion System," NASA Glenn Research Centre, Cleveland, OH, Report No. NASA-TM-2017-219501.
[36] Walsh, P. P., and Fletcher, P., 2004, *Gas Turbine Performance*, 2nd ed., Blackwell Science, Oxford, UK.
[37] Kawagishi, K., Yeh, A. C., Yokokawa, T., Kobayashi, T., Koizumi, Y., and Harada, H., 2012, "Development of an Oxidation-Resistant High-Strength Sixth-Generation Single-Crystal Superalloy TMS-238." In *Superalloys*, edited by E. S. Huron, R. C. Reed, M. C. Hardy, M. J. Mills, R. E. Montero, P. D. Portella, and J. Telesman, pp. 189–195.
[38] Bell, I. H., Wronski, J., Quoilin, S., and Lemort, V., 2014, "Pure and Pseudo-Pure Fluid Thermophysical Property Evaluation and the Open-Source Thermophysical Property Library CoolProp," Ind. Eng. Chem. Res., **53**(6), pp. 2498–2508.
[39] Lemmon, E. W., Bell, I. H., Huber, M. L., and McLinden, M. O., 2018, "NIST Standard Reference Database 23: Reference Fluid Thermodynamic and Transport Properties-REFPROP, Version 10.0," Software, National Institute of Standards and Technology, Gaithersburg, MD.
[40] Krempus, D., Bahamonde, S., van der Stelt, T. P., Klink, W., Colonna, P., and De Servi, C. M., 2024, "On Mixtures as Working Fluids of Air-Cooled ORC Bottoming Power Plants of Gas Turbines," Appl. Therm. Eng., **236**, p.121730.
[41] Astolfi, M., and Macchi, E., 2017, *Organic Rankine Cycle (ORC) Power Systems*, Woodhead Publishing, Duxford, UK.
[42] Sinopoli, F., Carandente, R., Schulz, Y., Krempus, D., Beltrame, F., De Servi, C. M., Nachtigal, P., Mimic, D., Colonna, P., and Pini, M., 2024, "Impact of the Working Fluid in ORC-Based Waste Heat Recovery Systems for Turboshaft Engines," Proceedings of Global Power and Propulsion Society, GPPS International Technical Conference 2024 (GPPS Chania 2024), Chania, Greece.
[43] Guillen, D. P., 2013, "Direct Evaporator Leak and Flammability Analysis—Modifications and Optimization of the Organic Rankine Cycle to Improve the Recovery of Waste Heat," Idaho National Laboratory (INL), Idaho Falls, ID, https://www.osti.gov/servlets/purl/1116740
[44] Kwak, H. D., Kwon, S., and Choi, C. H., 2018, "Performance Assessment of Electrically Driven Pump-Fed LOX/Kerosene Cycle Rocket Engine: Comparison With Gas Generator Cycle," Aerosp. Sci. Technol., **77**, pp. 67–82.
[45] Torenbeek, E., 1982, *Synthesis of Subsonic Airplane Design*, Delft University Press, Delft, The Netherlands.
[46] Sgueglia, A., Schmollgruber, P., Bartoli, N., Atinault, O., Benard, E., and Morlier, J., 2018, "Exploration and Sizing of a Large Passenger Aircraft With Distributed Ducted Electric Fans," AIAA Paper No. 2018-1745.
[47] Beltrame, F., 2026, "On the Preliminary Design of Aerospace-Grade Compact Heat Exchangers: From Ram Air Cooling Ducts to Energy Harvesting Systems," Ph.D. thesis, Delft University of Technology, Delft, The Netherlands.
[48] GRETh, 2023, "EchTherm Version 3.2," Software, NeoTherm Consulting SAS, La Motte-Servolex, France.
[49] Nichols, M. R., 1942, "Investigation of Flow Through an Intercooler Set at Various Angles to the Supply Duct," NACA Langley Memorial Aeronautical Laboratory, Hampton, VA, USA, Report No. 31176013639274.
[50] Kaltra GmbH, 2020, "Microchannel Condensers: Heat Exchangers for Condenser Applications," Kaltra GmbH, Munich, Germany, accessed June 16, 2023, https://www.kaltra.com/wp-content/uploads/2020/04/TM_Microchannel-Condensers_-Ver.3.0_EN.pdf
[51] Blank, J., and Deb, K., 2020, "Pymoo: Multi-Objective Optimization in Python," IEEE Access, **8**, pp. 89497–89509.
[52] Invernizzi, C. M., 2013, *Closed Power Cycles*, Springer, London, UK.
[53] Felder, J., Kim, H., and Brown, G., 2009, "Turboelectric Distributed Propulsion Engine Cycle Analysis for Hybrid-Wing-Body Aircraft," AIAA Paper No. 2009-1132.
[54] Schiltgen, B. T., and Freeman, J., 2016, "Aeropropulsive Interaction and Thermal System Integration Within the ECO-150: A Turboelectric Distributed Propulsion Airliner With Conventional Electric Machines," AIAA Paper No. 2016-4064.
[55] Oates, G. C., 1987, "Aerothermodynamics of Aircraft Gas Turbine Engines," U.S. Air Force Aero Propulsion Laboratory, Wright-Patterson Air Force Base, OH, Report No. AFAPL-TR-78-52.
[56] Lee, D. S., Fahey, D. W., Skowron, A., Allen, M. R., Burkhardt, U., Chen, Q., Doherty, S. J., et al., 2021, "The Contribution of Global Aviation to Anthropogenic Climate Forcing for 2000 to 2018," Atmos. Environ., **244**, p. 117834.
[57] Dallara, E. S., Kroo, I. M., and Waitz, I. A., 2011, "Metric for Comparing Lifetime Average Climate Impact of Aircraft," AIAA J., **49**(8), pp. 1600–1613.
[58] Proesmans, P., and Vos, R., 2022, "Airplane Design Optimization for Minimal Global Warming Impact," J. Aircr., **59**(5), pp. 1363–1381.

Downloaded from asmedigitalcollection.asme.org/gasturbinespower/article-pdf/148/11/111002/7625683/gtp-25-1623.pdf by Technische Universiteit Delft - Bibliotheek user on 20 October 2026